

The 100 pc White Dwarf Sample in the SDSS Footprint II. A New Look at the Spectral Evolution of White Dwarfs

MUKREMIN KILIC,¹ PIERRE BERGERON,² SIMON BLOUIN,³ ADAM MOSS,¹ WARREN R. BROWN,⁴ ANTOINE BÉDARD,⁵
GRACYN JEWETT,¹ AND MARCEL A. AGÜEROS⁶

¹*Homer L. Dodge Department of Physics and Astronomy, University of Oklahoma, 440 W. Brooks St., Norman, OK, 73019 USA*

²*Département de Physique, Université de Montréal, C.P. 6128, Succ. Centre-Ville, Montréal, QC H3C 3J7, Canada*

³*Department of Physics and Astronomy, University of Victoria, Victoria BC V8W 2Y2, Canada*

⁴*Center for Astrophysics, Harvard & Smithsonian, 60 Garden Street, Cambridge, MA 02138 USA*

⁵*Department of Physics, University of Warwick, CV4 7AL, Coventry, UK*

⁶*Department of Astronomy, Columbia University, 550 West 120th Street, New York, NY 10027, USA*

ABSTRACT

We increase the spectroscopic completeness of the 100 pc white dwarf sample in the SDSS footprint with 840 additional spectra. Our spectroscopy is 86% complete for white dwarfs hotter than $T_{\text{eff}} = 5000$ K, where H α remains visible and provides reliable constraints on the atmospheric composition. We identify 2108 DA white dwarfs with pure hydrogen atmospheres, and show that ultramassive DA white dwarfs with $M \geq 1.1 M_{\odot}$ are an order of magnitude less common below 10,000 K. This is consistent with a fraction of them getting stuck on the crystallization sequence due to ^{22}Ne distillation. In addition, there are no ultramassive DA white dwarfs with $M \geq 1.1 M_{\odot}$ and $T_{\text{eff}} \leq 6000$ K in our sample, likely because Debye cooling makes them rapidly fade away. We detect a significant trend in the fraction of He-atmosphere white dwarfs as a function of temperature; the fraction increases from 9% at 20,000 K to 32% at 6000 K. This provides direct evidence of convective mixing in cool DA white dwarfs. Finally, we detect a relatively tight sequence of low-mass DQ white dwarfs in color-magnitude diagrams for the first time. We discuss the implications of this tight DQ sequence, and conclude with a discussion of the future prospects from the upcoming ULTRASAT mission and the large-scale multi-fiber spectroscopic surveys.

1. INTRODUCTION

Gaia Data Release 2 (Gaia Collaboration et al. 2018) has unveiled the solar neighborhood white dwarf population in detail, and presented several puzzles that led to a revolution in our understanding of white dwarfs (Tremblay et al. 2024). Prior to Gaia, volume-limited white dwarf samples were limited to a few hundred stars within 20-25 pc (Holberg et al. 2016). Thanks to Gaia, it is now possible to create (nearly) complete volume limited samples with two orders of magnitude more stars (e.g., Jiménez-Esteban et al. 2018; Tremblay et al. 2020; Kilic et al. 2020; Gentile Fusillo et al. 2021; O’Brien et al. 2024).

The Gaia color-magnitude diagram revealed several unexpected features in the white dwarf sequence (Gaia Collaboration et al. 2018); the dominant A sequence is well matched by the predictions from the pure H atmosphere white dwarf models, but the split of the main branch into two (A and B), and the additional features like the Q-branch were surprising.

The bifurcation in the white dwarf sequence is due to atmospheric composition (Gaia Collaboration et al. 2018), but pure helium atmosphere models fail to match the location of the B-branch in color-magnitude diagrams. Bergeron et al. (2019) demonstrated that the solution to this problem could be the presence of trace amounts of hydrogen in helium-atmosphere white dwarfs. The presence of additional free electrons from trace elements in otherwise pure helium atmospheres increases the contribution of the He⁻ opacity, which changes the atmospheric structure and the continuum-forming region, shifting the location of the helium atmosphere white dwarfs in color-magnitude diagrams. The authors also mentioned that these additional free electrons could also come from carbon or other heavy elements. And indeed, recent evolutionary models and analyses based on GALEX far UV photometry demonstrated that convective dredge-up of optically undetectable (but UV detectable) traces of C from the interior can best account for the emergence of the B-branch

white dwarfs (Blouin et al. 2023a,b; Camisassa et al. 2023).

Tremblay et al. (2019b) provided a novel explanation for the over-density of the white dwarfs on the Q-branch as due to the cooling delays from the release of latent heat of crystallization. However, that alone is insufficient to explain the observed pile-up. Cheng et al. (2019) discovered a multi-Gyr cooling anomaly in 5-9% of massive white dwarfs, which implies that about half of the Q-branch population may belong to this delayed population. Blouin et al. (2021) and Bédard et al. (2024) showed that this anomaly is likely due to the ^{22}Ne distillation process that can cause up to about 10 Gyr cooling delays for massive white dwarfs.

Now that we understand the basics of the white dwarf sequence in Gaia color-magnitude diagrams, we can take advantage of volume-limited samples to obtain unbiased estimates of the white dwarf mass and luminosity functions. Until spectroscopic data from large multi-fiber robotic surveys like the SDSS-V and DESI become available (e.g. Manser et al. 2024), current volume-limited samples that are based on long-slit spectroscopy are limited to a few thousand objects. For example, the series of papers by Tremblay et al. (2020), McCleery et al. (2020), and O’Brien et al. (2023, 2024) obtained $> 99\%$ spectroscopic completeness for the 40 pc sample of 1081 objects.

In paper I of this series (Kilic et al. 2020), we took advantage of Gaia DR2 (Gaia Collaboration et al. 2018) and the prior spectroscopy from the SDSS, and provided follow-up spectroscopy of 711 additional white dwarfs to study the 100 pc white dwarf sample in the SDSS footprint. To make this survey feasible, our follow-up was limited to white dwarfs with $T_{\text{eff}} \geq 6000$ K, where atmospheric composition can be constrained through low-resolution spectroscopy. We achieved 59% spectroscopic completeness for the 4016 objects in this sample, with 83% completeness for white dwarfs hotter than 6000 K. This survey found that the DA mass distribution has an extremely narrow peak at $0.59 M_{\odot}$ with a shoulder from relatively massive white dwarfs with $M = 0.7 - 0.9 M_{\odot}$. Evolutionary models that include the cooling delays from the release of latent heat of crystallization, but without taking into account ^{22}Ne distillation, do not reproduce the pile-up of massive white dwarfs. This sample also revealed the presence of a well-defined sequence of infrared-faint (formerly classified as ultracool) white dwarfs (Bergeron et al. 2022).

Here we present the results from a new spectroscopic survey, where we push the temperature limit down to $T_{\text{eff}} = 5000$ K. Several important changes in cooling occur in the 5000-6000 K temperature range

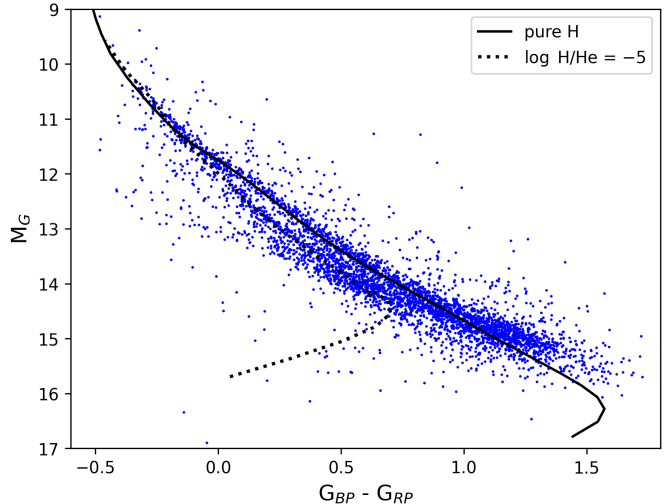


Figure 1. Color-magnitude diagram of the 100 pc white dwarf sample in the SDSS footprint. The solid and dotted lines show the evolutionary sequences for $0.6 M_{\odot}$ white dwarfs with pure H and mixed ($\log \text{H}/\text{He} = -5$) atmospheres down to $T_{\text{eff}} = 3000$ K, respectively.

(Saumon et al. 2022): the majority of white dwarfs have $M \approx 0.6 M_{\odot}$ and these stars go through crystallization. Therefore, this temperature range is essential for understanding the impact of crystallization and its associated effects (like ^{22}Ne distillation) on cooling for the most common white dwarfs. In addition, convective coupling between the convection zone and the degenerate interior occurs in the same temperature range, and massive white dwarfs enter the Debye cooling range, resulting in the rapid depletion of the thermal reservoir of the star. For reference, the spectroscopic completeness in the same temperature range is $\approx 20\%$ in Kilic et al. (2020).

We discuss our sample selection based on Gaia DR3 in Section 2, and provide the details of our spectroscopic follow-up in Section 3. We present the results from our detailed model atmosphere analysis in Section 4, and discuss the implications for the white dwarf mass distribution, spectral evolution, and cooling physics in Section 5. We conclude in Section 6.

2. SAMPLE SELECTION

Kilic et al. (2020) used Gaia DR2 astrometry to identify 4016 white dwarfs within 100 pc and the SDSS footprint. Our initial follow-up observations were based on this catalog. Since then, Gaia DR3 provided significantly improved astrometry given the longer baseline of the observations. We used the SDSS DR9 catalog and the Pan-STARRS DR1 catalog matched with Gaia

Table 1. Observational Details

Telescope	Instrument	Grating	Slit (")	Resolution (Å)	λ (Å)	Targets
APO 3.5m	KOSMOS	Blue VPH	2.1	4.7	4140 - 7030	15
FLWO 1.5m	FAST	300 l mm ⁻¹	1.5	3.6	3500 - 7400	12
Gemini South	GMOS	B600	1.0	5.5	3670 - 7100	84
Magellan 6.5m	MagE	175 l mm ⁻¹	0.85	1.0	3400 - 9400	4
MDM 2.4m	OSMOS	Blue VPH	1.2	3.3	3975 - 6865	357
MMT 6.5m	Blue Channel	500 l mm ⁻¹	1.25	4.8	3700 - 6850	368

DR3 to search for objects within 100 pc ($\varpi > 10$ mas) and 10σ significant parallax, G_{BP} , and G_{RP} photometry. We used a simple cut in the color-magnitude diagram, $M_G > 3.333 \times (G_{BP} - G_{RP}) + 8.333$, to select our white dwarf sample. In addition, we used the astrometric quality cuts given in equations 4, 5, and 8 in [Gentile Fusillo et al. \(2021\)](#) to obtain a clean sample. This selection is optimized for reliability rather than completeness. The color-magnitude selection keeps isolated (and unresolved double) white dwarfs, but removes the majority of the objects with main-sequence companions.

The final sample contains 4214 objects with G magnitudes ranging from 12.06 to 20.68. Given the improved astrometry from Gaia DR3, the sample size is slightly larger compared to [Kilic et al. \(2020\)](#). UV photometry can help distinguish between different atmospheric compositions ([Wall et al. 2023](#)). To take advantage of FUV and NUV photometry from GALEX, we propagated Gaia DR3 positions back to the GALEX epoch, and cross-matched with GUVcat ([Bianchi et al. 2017](#)) using a search radius of $3''$. We found 1605 targets (38% of the sample) with GALEX data.

We searched for spectroscopy for this sample in the SDSS, the Montreal White Dwarf Database (MWDD, [Dufour et al. 2017](#)), and the literature. We found 2244 objects with spectra available in the SDSS and MWDD (including the spectra from [Kilic et al. 2020](#)), and 62 additional objects with spectral types provided in the literature. Hence, 2306 objects (55% of the sample) have spectral classifications available in the literature.

Figure 1 shows the Gaia color-magnitude diagram for our white dwarf sample along with the evolutionary models for $0.6 M_{\odot}$ white dwarfs with pure H (solid line) and mixed ($\log H/He = -5$, dotted line) atmospheres ([Tremblay et al. 2011](#); [Blouin et al. 2019](#); [Bédard et al. 2020](#)). The bifurcation in the white dwarf sequence is clearly visible, and the hydrogen atmosphere model goes through the dominant A branch, though most white dwarfs redder than $G_{BP} - G_{RP} = 1.0$ appear to be over-

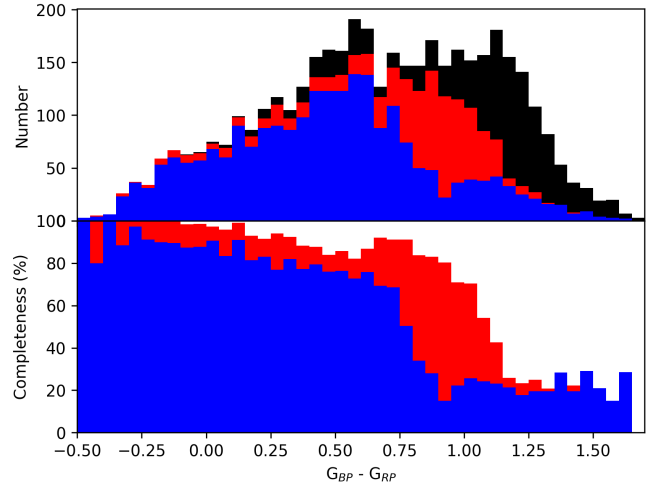


Figure 2. Color distribution of the 100 pc white dwarf sample in the SDSS footprint (black histogram, top panel), along with the completeness of the spectroscopic follow-up (bottom panel). The blue histogram shows the spectroscopically confirmed white dwarfs from the SDSS and the MWDD, whereas the red histogram shows the contribution from the new observations presented here.

luminous compared to the models. This is a known problem for cool white dwarfs (see [Caron et al. 2023](#); [O’Brien et al. 2024](#)). In addition, the model sequences make a blue turn for the faintest white dwarfs due to collision induced absorption from molecular hydrogen ([Hansen 1998](#)).

3. SPECTROSCOPIC FOLLOW-UP

We obtained optical spectroscopy of 840 white dwarfs using the 1.5m Fred Lawrence Whipple Observatory (FLWO), MDM Hiltner 2.4m, Apache Point Observatory (APO) 3.5m, 6.5m MMT, 6.5m Magellan, and 8m Gemini South telescopes. Table 1 presents the details of our observing program, including the instrument con-

Table 2. Physical Parameters of the 100 pc White Dwarfs in the SDSS footprint

SDSS name	Gaia Source ID	Type	Comp	Metals	T_{eff} (K)	Mass (M_{\odot})	$\log g$ (cm s^{-2})	M_{UNUV} (ABmag)
J000011.38−040315.1	2447815253423324544	DC	He	...	5207 ± 25	0.508 ± 0.012	7.897 ± 0.014	17.520
J000042.87+013221.7	2738626591386423424	DA	H	...	10055 ± 32	0.590 ± 0.006	7.983 ± 0.006	12.808
J000104.38+323704.0	2874216647336589568	DC	He	...	5707 ± 57	0.561 ± 0.030	7.984 ± 0.036	16.728
J000123.28−111155.9	2422442334689173376	DZA:	[H/He=−2.0]	[Ca/He=−10.79]	6531 ± 49	0.697 ± 0.017	8.195 ± 0.018	16.715
J000157.14+355947.0	2877080497170502144	DX	He	...	5448 ± 50	0.407 ± 0.022	7.702 ± 0.033	18.055
J000253.82+161036.0	2772241822943618176	DA	H	...	6756 ± 44	0.654 ± 0.023	8.102 ± 0.026	15.913
J000316.69−011117.9	2449594087142467712	DA	H	...	5372 ± 35	0.591 ± 0.023	8.013 ± 0.026	19.361
J000410.42−034008.5	2447889401738675072	DA	H	...	7066 ± 30	0.576 ± 0.007	7.973 ± 0.008	15.194
J000415.13+083840.5	2746843589674667264	DA	H	...	5981 ± 31	0.662 ± 0.015	8.120 ± 0.016	17.801
J000430.74+142958.7	2768919442402016896	DA	H	...	5164 ± 32	0.543 ± 0.032	7.936 ± 0.039	19.869

NOTE—This table is available in its entirety in machine-readable format in the online journal. A portion is shown here for guidance regarding its form and content. A bracket notation is used to characterize the ratio of the abundances in log scale. M_{UNUV} is the predicted absolute magnitude of each source in the ULTRASAT NUV band.

figuration and the number of targets observed at each telescope. These observations were obtained between 2020 October and 2024 May. MDM observations were obtained as part of the OSMOS queue, and Gemini data were taken as part of the queue programs GS-2022B-Q-304, GS-2023A-Q-227, and GS-2023A-Q-327. We make all of the spectra available on the MWDD (Dufour et al. 2017).

Combining our data with spectroscopy available in the SDSS and the MWDD, we have spectral classifications for 3146 (75%) of the 4214 white dwarfs in our sample. Figure 2 shows the number of spectroscopically confirmed white dwarfs (top panel), along with the completeness of the spectroscopic follow-up (bottom panel). The blue histogram shows the completeness of the spectroscopic follow-up based on the literature data available in the SDSS and MWDD, whereas the red histogram shows the contribution from the new observations presented here. The latter push the spectroscopic completeness to 100% for the bluest objects, and significantly improve the completeness for cool white dwarfs with $G_{\text{BP}} - G_{\text{RP}}$ colors up to 1.1. This color corresponds to $T_{\text{eff}} = 5000$ K for typical $M = 0.6 M_{\odot}$ pure hydrogen atmosphere white dwarfs. There are 3373 white dwarfs bluer than that color in our sample, including 2911 with spectra. Hence, our spectroscopic follow-up is 86% complete for white dwarfs with $T_{\text{eff}} \geq 5000$ K, and 91% complete for $T_{\text{eff}} \geq 6000$ K.

4. MODEL ATMOSPHERE ANALYSIS

4.1. The Photometric Method

We use the photometric technique as detailed in Bergeron et al. (2019) and Kilic et al. (2020). Briefly, we use the SDSS u and Pan-STARRS *grizy* photometry along with the Gaia DR3 parallaxes to constrain the effective temperature and the solid angle. Since the distance is known, we constrain the radius of the star directly, and use the white dwarf evolutionary models to calculate the mass. We include GALEX photometry, if available, to distinguish between the different atmospheric compositions, but not in the fits themselves. We ignore reddening since our sample is within 100 pc.

We convert the observed magnitudes into average fluxes, and compare with the synthetic fluxes calculated from model atmospheres with the appropriate chemical composition. We minimize the χ^2 difference between the observed and model fluxes over all bandpasses using the nonlinear least-squares method of Levenberg-Marquardt (Press et al. 1986) to obtain the best fitting parameters. The uncertainties of each fitted parameter are obtained directly from the covariance matrix of the fitting algorithm, while the uncertainties for all other quantities derived from these parameters are calculated by propagating in quadrature the appropriate measurement errors.

The details of our fitting method, including the model grids used are further discussed in Bergeron et al. (2019), Blouin et al. (2019), and Kilic et al. (2020). We rely on the evolutionary models from Bédard et al. (2020) with C/O cores, $q(\text{He}) \equiv M_{\text{He}}/M_{\star} = 10^{-2}$, and $q(\text{H}) = 10^{-4}$ and 10^{-10} , which are representative of H- and He-atmosphere white dwarfs, respectively.

4.2. DAs

There are 2121 DA white dwarfs in our sample, including 2108 normal DAs, 1 DAB, 1 DAQ, and 11 DAs with helium-dominated atmospheres. We refer the reader to [Sion et al. \(1983\)](#) for a detailed description of the white dwarf spectral classification system, and [Wesemael et al. \(1993\)](#) for an atlas of optical spectra of white dwarfs with different spectral types.

Figure 3 shows our model fits to a typical cool DA, where only a weak H α line is observed. The top panel shows the SDSS *u* and Pan-STARRS *grizy* photometry (error bars) along with the predicted fluxes from the best-fitting pure H (filled dots) and pure He (open circles) atmosphere models. The labels in the same panel give the SDSS name, Gaia Source ID, and the photometry used in the fitting. Here and in the following figures, any excluded bandpasses are shown in red. Clearly, photometry alone cannot distinguish between the two models. The middle panel shows the predicted spectrum based on the pure hydrogen solution, along with the observed H α line. This is not a fit to the line profile, we simply over-plot the predicted hydrogen line (red line) from the photometric fit. The bottom panel shows a broader spectral range. The photometric fit provides an excellent match to the H α line for this white dwarf, confirming that this is a pure hydrogen atmosphere white dwarf with $T_{\text{eff}} = 5694$ K and $M = 0.546 M_{\odot}$.

We provide the model fits for all spectroscopically confirmed white dwarfs in our sample on Zenodo, which can be accessed via the DOI [10.5281/zenodo.13799326](https://doi.org/10.5281/zenodo.13799326). Table 2 presents the physical parameters for each object, including the SDSS names and Gaia source IDs. We refer to each object using their shortened SDSS names, e.g. J0000–0403 for the first object in the table. Model fits for magnetic white dwarfs will be presented in an accompanying paper by Moss et al. (in prep). Nearly all of the DAs in our sample have spectra that are well-matched by pure H atmosphere models, but there are exceptions. Here we concentrate on two types of unusual objects: He-rich DAs and DAs in suspected double degenerate systems.

We identify 11 DA white dwarfs where the spectral energy distributions and observed spectra are better-reproduced by He-dominated atmospheres. Even though He becomes invisible below 11,000 K, its presence can still be inferred from the spectral energy distribution and the shape of the H lines, as they are heavily broadened through van der Waals interactions in helium-dominated atmospheres ([Bergeron et al. 2001](#); [Rolland et al. 2018](#)). [Kilic et al. \(2020\)](#) referred to these objects as DA(He). However, to avoid confusion with the recently identified class of magnetic white dwarfs

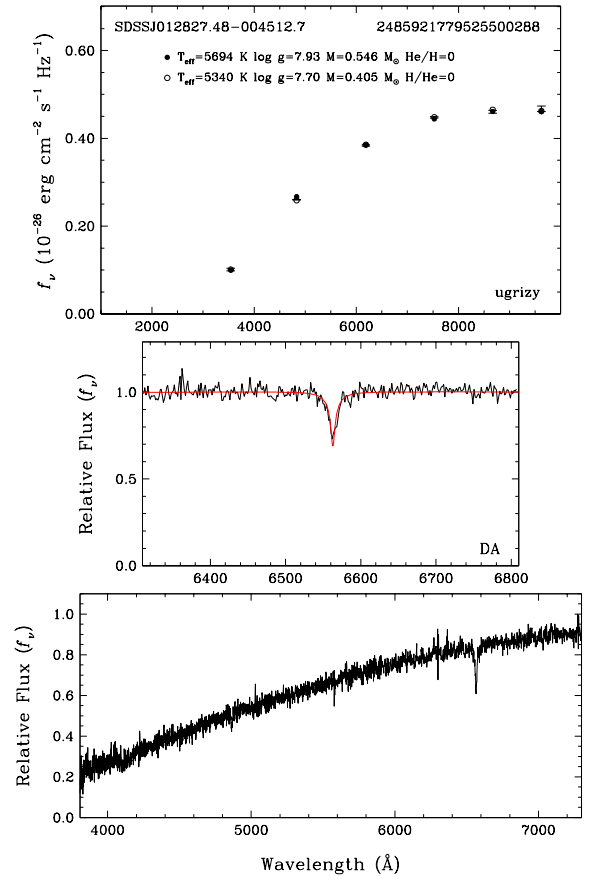


Figure 3. Model fits to the cool DA white dwarf SDSS J012827.48–004512.7. The top panel shows the best-fitting pure H (filled dots) and pure He (open circles) atmosphere white dwarf models to the photometry (error bars). This panel also includes the SDSS name and the Gaia Source ID, and the photometry used in the fitting. The middle panel shows the predicted spectrum (red line) based on the pure H solution. The bottom panel shows a broader wavelength range. Here the photometry cannot distinguish between H- and He-atmospheres for this relatively cool white dwarf. However, spectroscopy clearly indicates that this is a pure H atmosphere white dwarf.

with emission lines, DAHe (e.g., [Gänsicke et al. 2020](#)), we refer to He-rich DAs as He-DAs.

Figure 4 shows our model fits to the He-DA white dwarf J1529+1304. Even though J1529+1304 is nearly 5000 K hotter than the cool DA shown in Figure 3, their optical spectra look similar with only a weak H α feature visible. In addition, the spectral energy distribution for J1529+1304 (top panel) clearly favors a He-dominated solution. A He-dominated atmosphere model with $T_{\text{eff}} = 9228$ K and $\log \text{H}/\text{He} = -4$ provides an excellent match to both the photometry and the H α line profile (middle panel). In addition, this model does not predict any other visible Balmer lines, just like in the observed spectrum shown in the bottom panel.

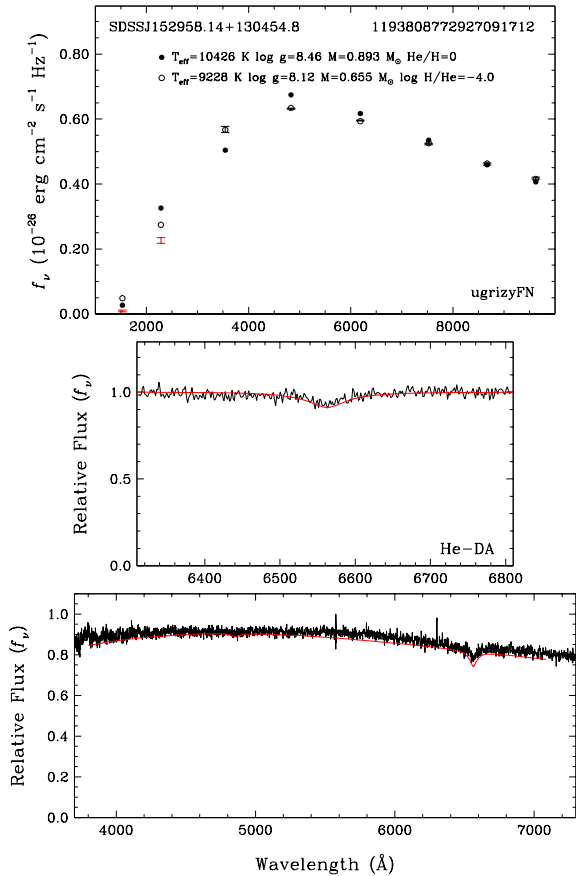


Figure 4. Model fits to the He-DA white dwarf SDSS J152958.14+130454.8. If this was a regular DA white dwarf, its spectrum would have been dominated by the Balmer lines, instead we only see a weak H α feature even though this white dwarf is hotter than 9000 K. The spectral energy distribution and the observed H α line profile (middle and bottom panels) are best-explained by a He-dominated atmosphere with trace amounts of H.

Note that there are four DA white dwarfs in our sample, J1611+1322, J1628+1224, J2104+2333, and J2138+2309, that were erroneously classified as He-DA in Kilic et al. (2020). Even though the photometry favors a helium-dominated solution for these four objects, unlike the other 11 He-DA in our sample, the complete Balmer series is visible in their spectra. Indeed, the predicted Balmer line profiles based on the parameters obtained from the pure H photometric solutions are entirely consistent with the overall spectra, indicating that the observed photometry is inconsistent with the observed spectra. Caron et al. (2023) also highlighted J1611+1322 and J2138+2309 as unusual DA white dwarfs where they achieve a better fit to the photometry using He-dominated atmosphere models. It is unclear why there is a discrepancy, but one possibility is that the discrepant photometric and spectroscopic pa-

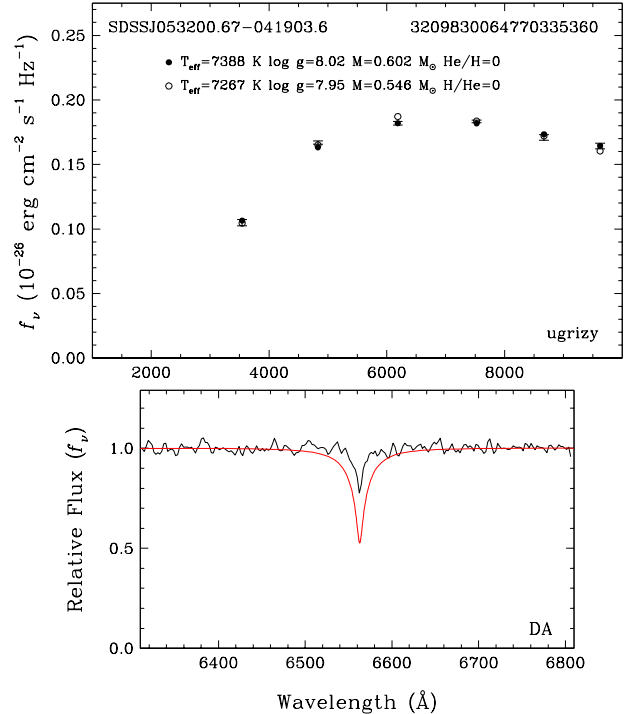


Figure 5. Model fits to the suspected double degenerate binary system SDSS J053200.67–041903.6. The relatively weak H α line could be explained by contribution from a DC white dwarf companion.

rameters are due to additional light from an unresolved white dwarf companion (Bédard et al. 2017). We thus reclassify these objects as DA stars.

Another object in the sample, J1159+0007, shows asymmetric Balmer line profiles and its photometry and H α spectrum favor a He-dominated atmosphere. J1159+0007 is very similar to another white dwarf with asymmetric Balmer lines, J0103–0522, analyzed by Caron et al. (2023). Even though both objects are massive ($M \sim 1.0 M_{\odot}$) and have relatively weak Balmer lines, we realized that the predicted Balmer line spectra obtained from the He-dominated solutions are actually inconsistent with the observed spectra. Tremblay et al. (2020) classified J0103–0522 as a potentially magnetic DAH: white dwarf. Caron et al. (2023) suggest that instead of magnetism, the asymmetric profiles may be because of some unaccounted line broadening due to helium. We currently do not have a favored explanation for these asymmetric line profiles, though we confirm that He-DA models do not match the observed spectra, and we thus reclassified J1159+0007 as a DA white dwarf.

In addition to the He-rich and the unusual DAs discussed above, there are a dozen other DAs where the photometry favors the H-rich solution, but the predicted H α line profiles are significantly different than expected.

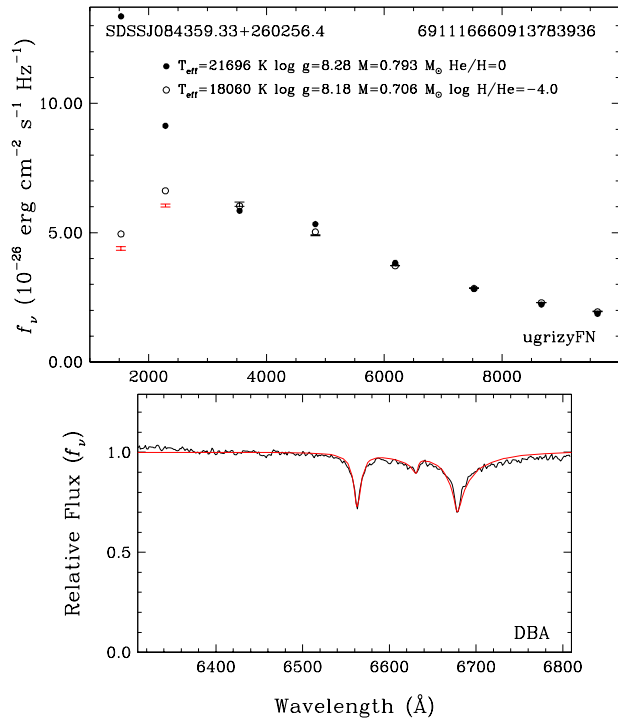


Figure 6. Model atmosphere fits to the DBA white dwarf Ton 10. The top panel shows the photometric fit, and the bottom panel shows that a model with $\log \text{H}/\text{He} = -4$ provides an excellent match to the observed spectrum in the H α region.

Figure 5 shows the model fits for one of these systems, J0532–0419. The photometric method indicates a pure H atmosphere white dwarf with $T_{\text{eff}} = 7388 \text{ K}$ and $M = 0.602 M_\odot$. However, the observed H α line profile is significantly weaker than expected. Note that this is not due to magnetism or a He-dominated atmosphere, as the line is relatively sharp and there is no evidence of Zeeman splitting in the spectrum. On the other hand, additional light from a DC white dwarf could explain the relatively weak H α feature in this system. We classify this object, and 11 others (J0611+0544, J1022+4600, J1033+0621, J1234+1503, J1243+6712, J1442+0027, J1555+0647, J1857+2026, J2045–0016, J2138+1123, J2229+3024), as suspected double degenerates. Several of these systems are low-mass ($M < 0.5 M_\odot$), which also favors a binary formation channel (Marsh et al. 1995; Munday et al. 2024). Others may still be double degenerates, but with more massive components.

4.3. DBs

There are 50 DB white dwarfs in our sample, including 35 that also show H absorption features. We use the DB model atmospheres described in Bergeron et al. (2011) and Genest-Beaulieu & Bergeron (2019). We use the photometric technique to determine the best-fit tem-

perature and surface gravity for these stars, and use H α (if visible) to constrain the H/He ratio. Our model grid includes atmosphere models with pure He composition and $\log \text{H}/\text{He} = -6$ to -2 with 0.5 dex resolution. If no H features are visible, we assume a pure He atmosphere composition. This is a valid approximation for DBs as adding H at the visibility limit barely changes the derived parameters (Genest-Beaulieu & Bergeron 2019).

Figure 6 shows our model fits to the DBA white dwarf J0843+2602 (Ton 10), which displays a significant H α absorption feature. The photometric fit (top panel) shows that this is a $T_{\text{eff}} = 18060 \text{ K}$ and $M = 0.706 M_\odot$ white dwarf. The bottom panel demonstrates that a model with $\log \text{H}/\text{He} = -4$ provides an excellent match to both the H and He lines visible in the spectrum of this star. We find H/He ratios ranging from -6 to -3.5 for the DBA white dwarfs in our sample.

4.4. DCs

There are 715 white dwarfs in our sample with featureless spectra and with $T_{\text{eff}} \leq 12,000 \text{ K}$. Above this temperature, DC white dwarfs would have to be strongly magnetic for their absorption lines to be shifted and distorted to create a featureless spectrum. Below this temperature, He becomes invisible, but H remains visible down to $\sim 5000 \text{ K}$, below which H also becomes invisible, except in IR-faint white dwarfs that show collision induced absorption due to molecular hydrogen. Hence, a spectrum alone is insufficient to determine the atmospheric composition for the coolest DC white dwarfs.

As discussed previously, the location of the B-branch in the Gaia color-magnitude diagram requires DC white dwarfs to have trace amounts of H, C, or other electron donors in their atmospheres (e.g., Bergeron et al. 2019). Blouin et al. (2023a), Blouin et al. (2023b), and Camisassa et al. (2023) further demonstrated that C is likely the culprit, and that optically undetectable trace amounts of C dredged up from the interior would shift the colors of He atmosphere white dwarfs. They also concluded that the use of model atmospheres with trace H as a proxy for all electron donors is likely appropriate for the analysis of the DC white dwarfs, although this has not been demonstrated quantitatively.

Figure 7 shows the masses and temperatures for DC white dwarfs under the assumption of various atmospheric compositions, shown by red circles. In each panel, pure He atmosphere model fits are shown as open circles and serve as a reference. As better seen in the bottom panel, these pure He solutions yield masses that are overestimated, as first noted by Bergeron et al. (2019). In contrast, models including traces of hydrogen (top two panels) show a mass distribution much

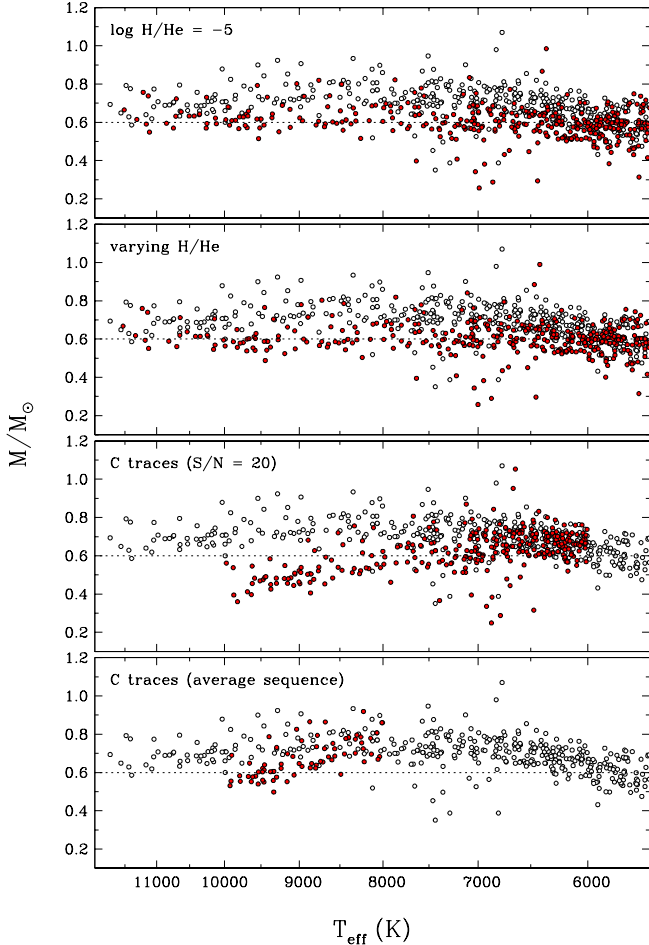


Figure 7. Masses for the DC white dwarfs in our sample under the assumption of various atmospheric compositions. In each panel, the pure helium model fits are shown as open circles, while the solutions obtained by including trace elements indicated in the figure are shown as red circles. The second panel from the top (labeled varying H/He) shows the results where the H/He abundance ratio was adjusted as a function of T_{eff} following the predictions of the convective mixing scenario of Rolland et al. (2018).

closer to the canonical $0.6 M_{\odot}$ value. We limit the comparisons between the mixed H/He atmosphere models to $T_{\text{eff}} \geq 5500$ K, as the collision induced absorption from molecular hydrogen dominates the opacity in the near-infrared for cooler mixed atmosphere white dwarfs (Bergeron et al. 2022).

Both Kilic et al. (2020) and Caron et al. (2023) adopted He-rich models to fit the DC stars in their sample, where the H/He abundance ratio was adjusted as a function of T_{eff} following the predictions of the convective mixing scenario of Rolland et al. (2018). This is the approximation shown in the second panel of Figure 7. Several other groups used instead a fixed value of $\log \text{H/He} = -5$ to fit DC stars (e.g., Gentile Fusillo et al.

2021; Jiménez-Esteban et al. 2023; O’Brien et al. 2024). Interestingly, the solutions for He atmosphere model fits with a fixed value of $\log \text{H/He} = -5$ (top panel) are essentially identical to the fits with varying H/He ratios used. We adopted solutions for DC white dwarfs following the same strategy as in Caron et al. (2023), and use mixed H/He models where the H abundance is adjusted as a function of effective temperature for objects hotter than $T_{\text{eff}} = 5200$ K, while for the 5200-6500 K temperature range, we adopt the pure He or mixed H/He solution based on a χ^2 analysis (see Section 3.7 of Caron et al. 2023 for a full discussion of these approximations).

The bottom two panels of Figure 7 show the results where traces of carbon are used instead of hydrogen. We postpone the discussion of these results to Section 5.5.

4.5. IR-faint White Dwarfs

Our sample includes 37 IR-faint white dwarfs identified by Bergeron et al. (2022), including 23 IR-faint DCs, 1 DQ, and 1 DZ. The remaining 12 targets were missing spectroscopic follow-up. We were able to obtain spectroscopy of seven of the targets with missing spectral classification, and confirm all of them to be DC white dwarfs; J0035+2009, J0146+2122, J1448+2935, J1546+2054, J1639+0106, J2237+2220, and J2332+0959. We adopt the fits provided by Bergeron et al. (2022), which include infrared photometry.

4.6. DQs

There are 127 DQ white dwarfs in our sample, with the majority of them belonging to the cool DQ population with $T_{\text{eff}} < 10,000$ K. We use the photometric technique to determine the best-fit temperature and surface gravity for these stars, and use the C_2 Swan bands and/or the C I lines to fit for C/He. Given the abundances derived from the spectroscopic fit, we repeat our photometric and spectroscopic fits until a consistent solution is found. We omit the SDSS u -band photometry in our model fits for the DQs due to the potential problems with the C opacities in the UV (e.g., CouTu et al. 2019).

Figure 8 shows our model fits to two of these stars. Model fits to J1028+3512 (left panels) are excellent; He-dominated atmosphere models with trace amounts of C provide an excellent match to the observed spectral energy distribution from the UV to the near-infrared. The right panels show the model fits to a magnetic DQ. These fits are also very good; J1333+0016 shows broad and rounded molecular absorption features in the optical, and besides the issues with matching the u -band

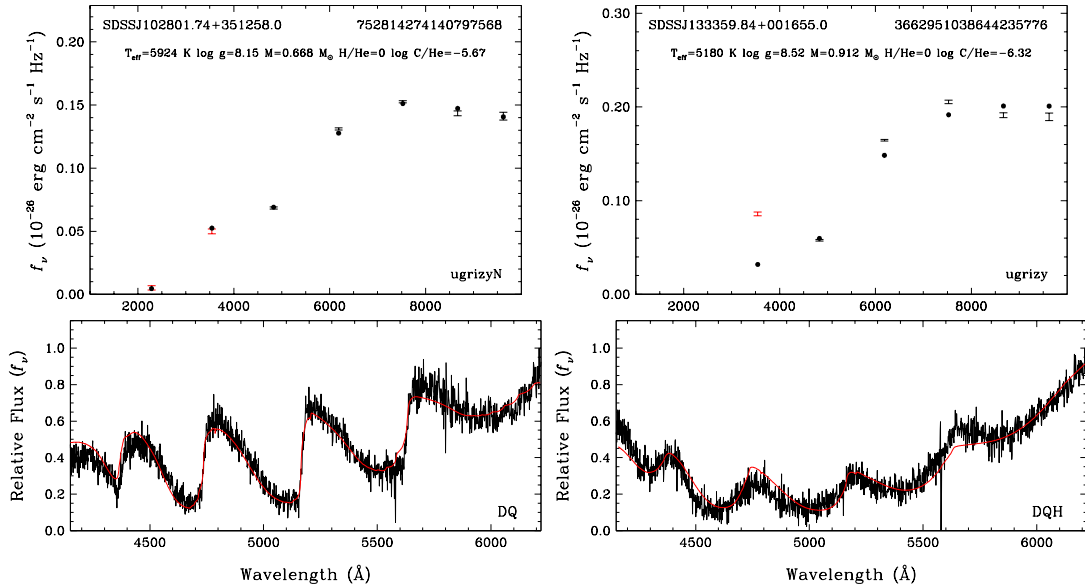


Figure 8. Model fits to the DQ white dwarfs SDSS J102801.74+351258.0 (left) and SDSS J133359.84+001655.0 (right). The atmospheric models provide an excellent match to both photometry and spectroscopy for these two stars, one of which is magnetic (right panels).

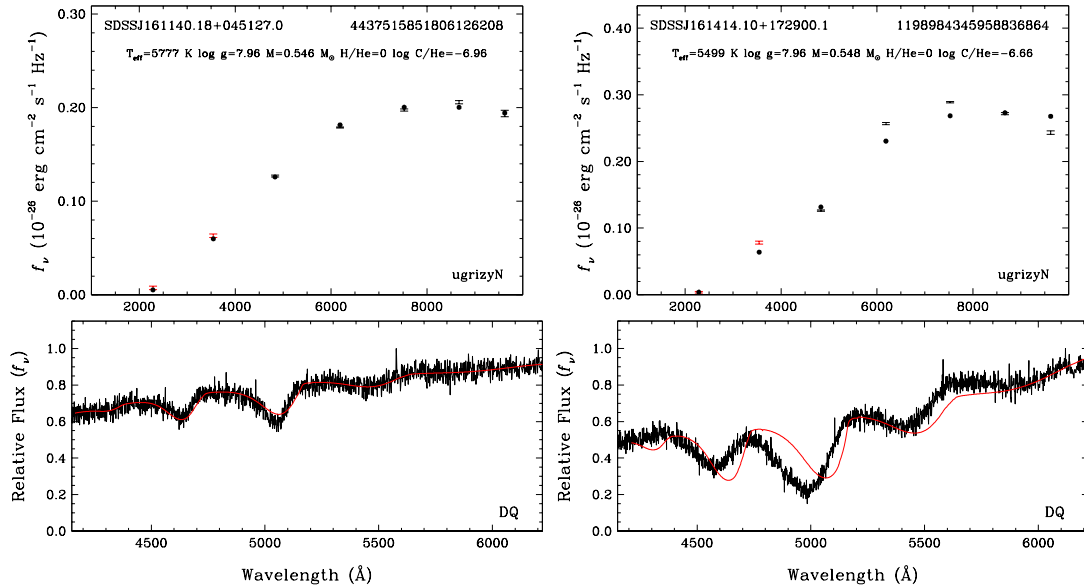


Figure 9. Model fits to two DQ white dwarfs with pressure-shifted Swan bands. We obtain good fits for SDSS J161140.18+045127.0 (left panels), but not for SDSS J161414.10+172900.1 (right panels).

photometry, the models provide a good match to the Swan bands. The majority of the DQs in our sample have fits similar to the ones shown in this figure. Here we highlight three types of outliers among the DQ population.

Figure 9 shows our fits to two DQ white dwarfs with shifted molecular bands. Kowalski (2010) demonstrated that the shifted bands are most likely the pressure-shifted bands of C_2 in the fluid-like atmospheres of cool DQ white dwarfs. Blouin & Dufour (2019) were

able to obtain very good fits by including a density-driven shift of the electronic transition energy of the Swan bands as found by Kowalski (2010). Here we rely on the same models to fit cool DQs with shifted Swan bands. These models provide a good match to the observed spectrum of J1611+0451 (left panels), but fail for J1614+1729 (right panels). We find three other DQs with similar problems, J1159+1300, J1835+6429, and J2232–0744. The models predict C_2 bands that are not shifted enough, likely because the atmospheric pressure

is underestimated. [Blouin & Dufour \(2019\)](#) note that the origin of this problem is unclear, as the models with shifted Swan bands fit most but not all of these targets. They suggest that the empirically determined density-driven shifts may not be accurate for all objects or that the problem objects may be magnetic. Magnetism can impact the atmospheric structure by suppressing convection, and distorting the Swan bands, though it is not clear why this is not a problem for the magnetic DQ J1333+0016 shown in [Figure 8](#).

The second set of outliers among the DQ population involves five warm DQs with temperatures ranging from about 12,000 K to 16,000 K. Warm DQs are significantly more massive than the more common cool DQs in the solar neighborhood ([Dufour et al. 2008](#); [Coutu et al. 2019](#); [Koester & Kepler 2019](#)), and their physical parameters, kinematics, and location on the Q-branch favor a white dwarf merger origin ([Dunlap & Clemens 2015](#); [Kawka et al. 2023](#); [Kilic et al. 2024](#)). They are likely stuck on the crystallization sequence due to ^{22}Ne distillation ([Bédard et al. 2024](#); [Jewett et al. 2024](#)). [Kilic et al. \(2024\)](#) show that because the He line at 5876 Å is never observed in warm DQs, it is impossible to constrain the He abundance in their atmospheres. Instead, we can only put upper limits on the He abundance, as atmosphere models with no He provide model fits that are comparable to the fits including He. As in [Kilic et al. \(2024\)](#), we use a model grid with a fixed value of $\log C/\text{He} = 0$ to fit warm DQs, and then fit for H/He to match H α in DQA white dwarfs (see also [Jewett et al. 2024](#)).

Slightly cooler than the warm DQ population, we find five other unusually massive DQs with $M \geq 0.87 M_{\odot}$ and $T_{\text{eff}} = 8450 - 11,060$ K. Three of these objects show both molecular and atomic C absorption features; J0859+3257, J1140+1824, J1148-0126. The left panels in [Figure 10](#) show the model fits to J1140+1824. The photometric method finds the best-fitting parameters of $T_{\text{eff}} = 10,111$ K, $M = 0.87 M_{\odot}$, and $\log C/\text{He} = -3.17$, which provides a decent match to the molecular features in the spectrum. However, this model severely underpredicts the depth of the atomic C lines; the best-fitting model temperature is too low. This is a manifestation of the known problem that molecular and atomic C absorption features generally cannot be reproduced simultaneously when both are visible ([Dufour et al. 2005](#)). One possibility is that there is something wrong with the UV opacities (there are many C lines in the UV), which affect the entire spectrum in a way that leads to the wrong photometric temperature (and hence C/C₂ balance). In particular, there are strong UV lines which are predicted to extend far into the visible (based on

simple Lorentzian profiles), similar to the Lyman α in cool DAs ([Kowalski & Saumon 2006](#)).

The right panels in [Fig. 10](#) show the model fits to the same object where we arbitrarily increased the effective temperature to 11,000 K. We obtain much better fits to the observed spectrum if the temperature is about 1000 K hotter than indicated by the photometry, and the mass is also about 0.1 M_{\odot} higher. With effective temperatures above 10,000 K and masses near 1 M_{\odot} , these stars are significantly more massive than the cool DQs ([Blouin et al. 2019](#)). They are also located on the Q-branch (see [Figure 14](#) below). Hence, these stars seem to form the lower-temperature and lower-mass continuation of warm DQs.

4.7. DZs

There are 130 DZ white dwarfs in our sample that display metal absorption lines, mainly Ca II H and K. We rely on the photometric technique to determine the temperature and surface gravity for these stars, and fit the blue portion of the spectrum to constrain Ca/He. The abundance ratios of the other heavy elements are assumed to match the CI chondrites. We use the H α region, when available, to constrain the H/He abundance ratio. In some cases, it is also possible to constrain this ratio by looking at the overall quality of the fits to the energy distribution and optical spectrum.

[Figure 11](#) shows our model fits to two DZ white dwarfs. The left panels show the fits to the DZA white dwarf J0141+2257, which shows strong lines of Mg, Na, and H. An atmosphere model with $T_{\text{eff}} = 7727$ K, $M = 0.635 M_{\odot}$, and $\log \text{Ca}/\text{He} = -7.74$ (along with the chondritic metal abundance ratios) provides an excellent match to the photometry and spectroscopy for this object. The only noticeable difference between the model and the observations is the depth of the Mg triplet near 5175 Å. Cool DZ white dwarfs are known to have higher Mg/Ca ratios on average than the chondritic ratio ([Blouin 2020](#)), likely because of the slower sinking timescale of Mg compared to Ca. Even though these model fits could be improved by fitting for the abundance ratios of each element, this is beyond the scope of this paper.

The right panels show our model fits for the DZ white dwarf J2357+1949. We adopt in this specific case the H/He = 0 solution, which provides the best fit to the overall photometric and spectroscopic data. The best-fitting model with $\log \text{Ca}/\text{He} = -8.19$ provides a remarkable fit to the observed spectrum of this object. Again, there are some issues with matching the Mg feature due to our assumption of the chondritic abundance ratios, but otherwise the fit is essentially perfect. We

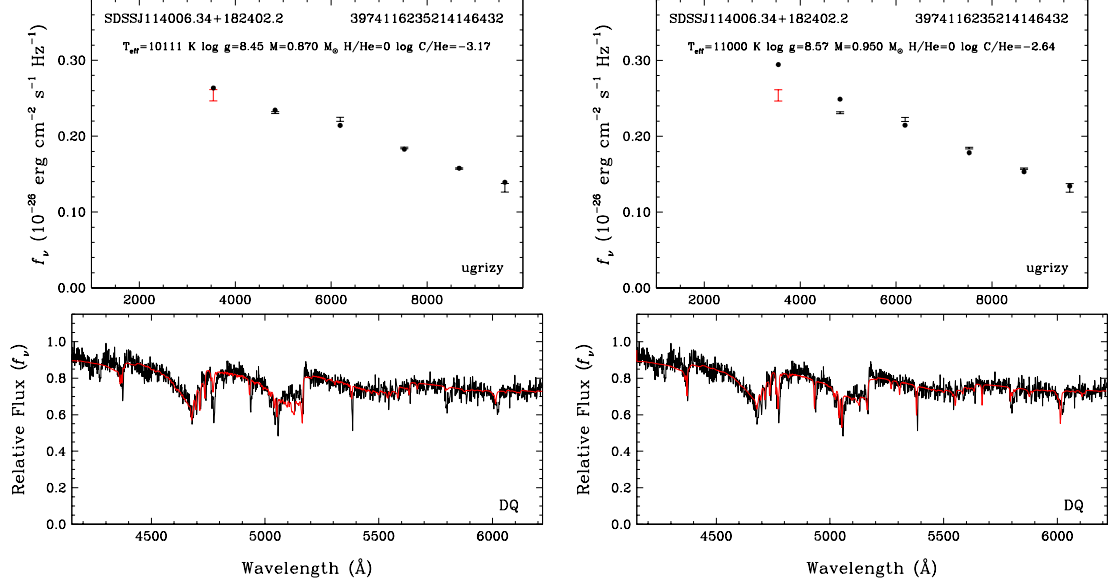


Figure 10. Model fits to the DQ white dwarf SDSS J114006.34+182402.2, which displays both molecular and atomic C lines. The left panels show the results from the photometric fits, whereas the right panels show a model fit where we arbitrarily increased the effective temperature to 11,000 K.

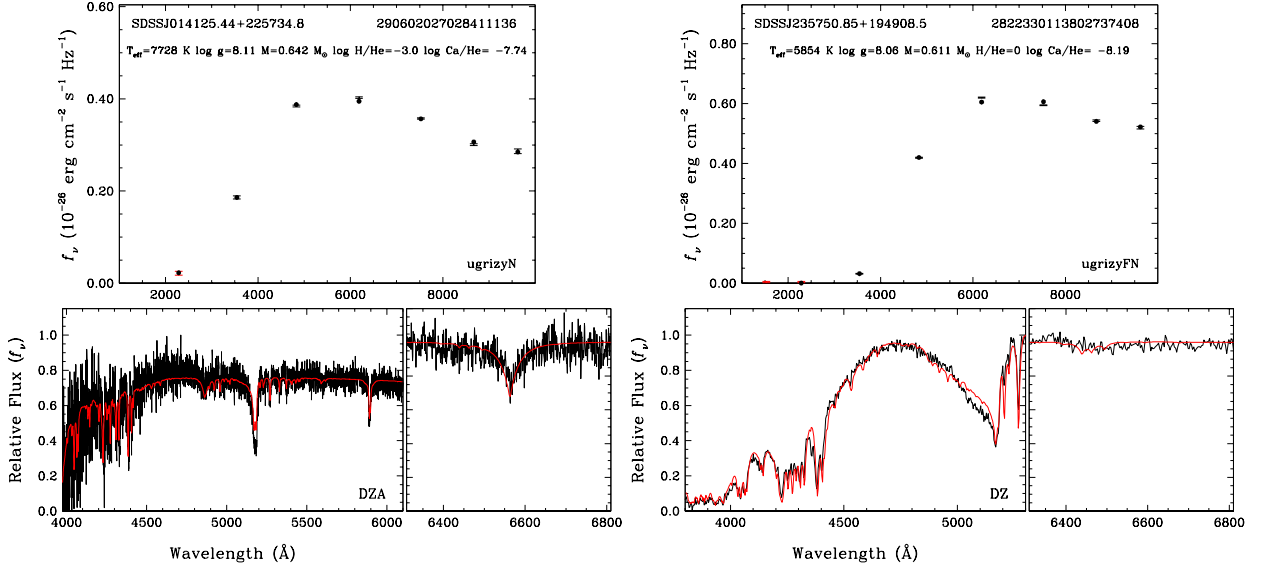


Figure 11. Model fits to the DZA white dwarf SDSS J014125.44+225734.8 (left panels) and the DZ SDSS J235750.85+194908.5 (right panels). The top and bottom panels show the photometric and spectroscopic model fits, respectively.

find a relatively wide range of H/He ratios for the DZ white dwarfs in our sample, including some with no hydrogen.

Among the DZ white dwarf population, we identify seven magnetic objects, four of which are new discoveries. Figure 12 shows the MDM and MMT spectra for these four targets, which clearly show metal line triplets. Zeeman split Na lines near 5890 Å are clearly visible in J1406+2224, J2105+0900, and J2357+2747, and split Mg lines near 5170 Å are visible in J1543-0247.

J2105+0900 also shows the split Ca I line at 4227 Å. Modeling the magnetic field structure of these stars beyond the scope of this paper. Even though the DZ white dwarfs in our sample span the temperature range of 4260 - 12,000 K, all but one of the magnetic DZs are found in a relatively narrow temperature range of 5340 to 6560 K. The exception is the coolest DZH in our sample, J2105+0900, which has $T_{\text{eff}} = 4427$ K.

4.8. DX

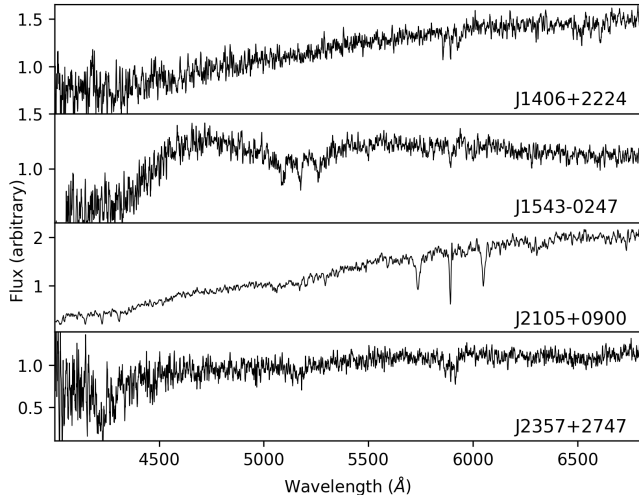


Figure 12. Spectra for the newly identified DZH white dwarfs in our sample.

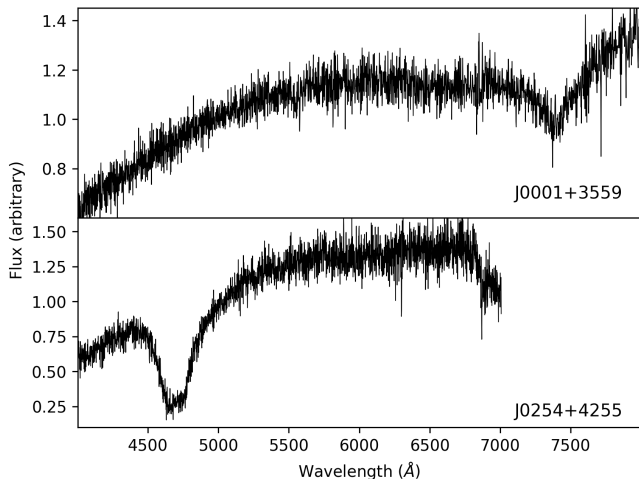


Figure 13. Spectra for two white dwarfs with an unknown spectral type (classified as DX).

We are not able to classify two of the targets based on the available data. Figure 13 shows the spectra for those two targets. J0001+3559 shows a featureless spectrum except for a broad feature around 7400 Å. It was classified as a DC and a DZ in the literature (Kepler et al. 2019; Caron et al. 2023). Its overall spectral energy distribution is consistent with a $T_{\text{eff}} \approx 6600$ K and $M = 0.46 M_{\odot}$ white dwarf. We find that its spectrum is similar to the DXP white dwarf GJ 1221. We cannot confidently assign a spectral type to J0001+3559 and polarization measurements are unavailable, hence we classify it as a DX white dwarf that requires further analysis to understand its nature. The second target, J0254+4255, has $T_{\text{eff}} \approx 5400$ K, and it displays a broad and deep absorption feature around 4700 Å. Given its

relatively cool temperature, magnetically shifted H or He lines cannot explain the observed spectrum, and its spectral type remains uncertain.

5. DISCUSSION

5.1. The White Dwarf Sequence in the H-R diagram

Gaia DR2 and DR3 provided a detailed map of the white dwarf sequence in the Hertzsprung-Russell diagram for the first time, and revealed three main branches labeled as A, B, and Q (Gaia Collaboration et al. 2018). Here, Q stands for ‘Question’, as the appearance of the Q-branch was neither expected nor understood at the time (M. Barstow 2024, private communication). Figure 14 shows color-magnitude diagrams of the spectroscopically confirmed white dwarfs presented in this work. Here, we also label the fourth branch, the IR-faint white dwarf sequence in the left panel, first identified by Kilic et al. (2020) and studied in detail by Bergeron et al. (2022).

The right panel in Figure 14 shows the DA only sample. $H\alpha$ becomes invisible below about $T_{\text{eff}} = 5000$ K, which corresponds to $g - z = 1.0$. Hence, the DA sample is limited to bluer objects. The A-branch is mainly made up of $M \approx 0.6 M_{\odot}$ DA white dwarfs, though DA white dwarfs are found both above and below the A-branch due to the contribution from low- and high-mass DA white dwarfs, respectively. The B-branch is mainly made up of DC, DQ, and DZ stars, whereas the Q-branch consists of massive DA and DQ white dwarfs on the crystallization sequence (Cheng et al. 2019; Jewett et al. 2024). Even though warm and massive DQs are over-represented on the Q-branch because they appear to be stuck there (Cheng et al. 2019; Blouin et al. 2021; Bédard et al. 2024; Jewett et al. 2024), the majority of the DQ white dwarfs are actually found on the B-branch.

The left panel in Figure 14 reveals a relatively tight sequence for DQ white dwarfs. In addition to the warm DQs on the Q-branch, cooler DQs on the B-branch also seem to form a tight sequence. To our knowledge, this is the first time such a tight DQ sequence is identified in color-magnitude diagrams. On average, DQ white dwarfs are brighter and/or redder than DZ white dwarfs in this diagram. At first glance, this difference between DQ and DZ white dwarfs may be attributed to the additional absorption from the C_2 Swan bands in DQ white dwarfs in the g -band, making their $g - z$ colors redder than their DZ counterparts. However, the difference between DQs and DZs is obvious even at $g - z < 0$, where the Swan bands are relatively weak. Furthermore, this distinction is present in other filters, too.

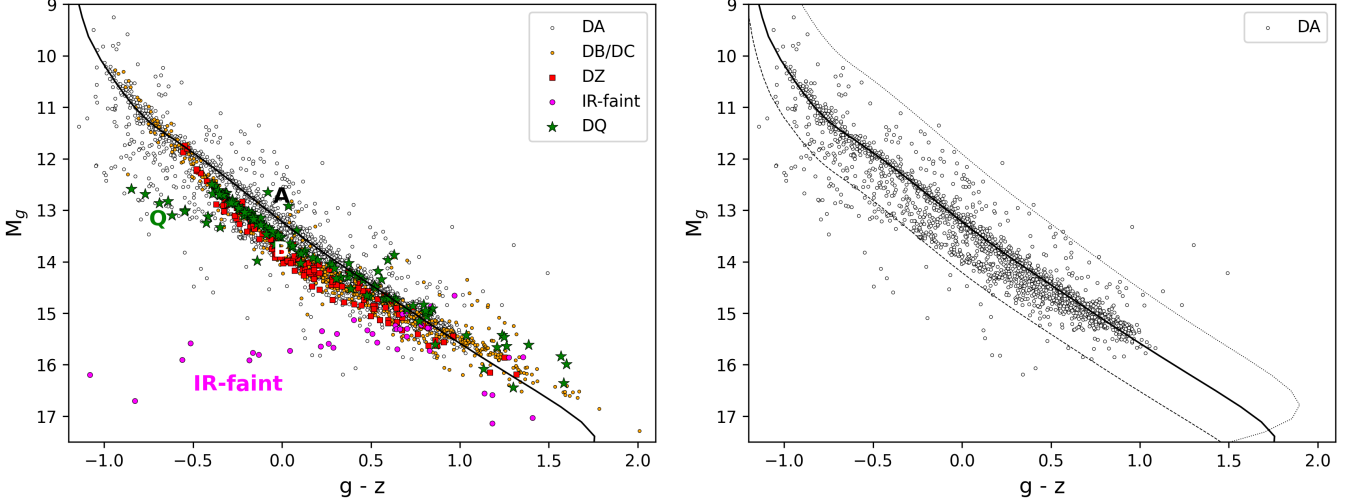


Figure 14. Color-magnitude diagrams of the spectroscopically confirmed white dwarfs in the 100 pc sample and the SDSS footprint. The right panel includes the evolutionary sequences for 0.2, 0.6 (solid line, also shown in the left-panel), and 1.0 M_{\odot} pure H atmosphere white dwarfs (top to bottom).

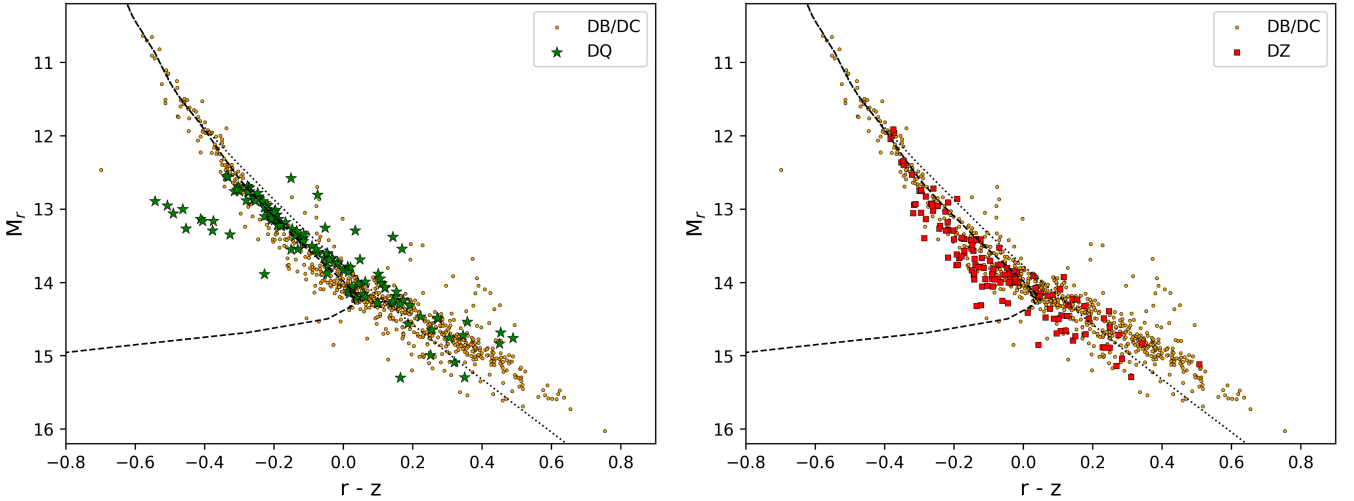


Figure 15. Color-magnitude diagrams of the DB/DC (orange), DQ (green stars), DZ (red squares), along with the evolutionary sequences for pure He (dotted) and mixed H/He atmosphere white dwarfs with $\log H/He = -5$.

Figure 15 shows another color-magnitude diagram where we use the Pan-STARRS r filter instead. Here we show a comparison between the DB/DC sequence versus DQ (left) and DZ (right) white dwarfs. DZs fall along the DC white dwarf sequence, but the DQs are restricted to a tight sequence here as well, and on average, they are brighter. This is likely because of significant differences in the mass distributions of each population (see section 5.5).

We close this section by highlighting the utility of the SDSS u -band for the identification of the coolest DQ white dwarfs in the solar neighborhood. Figure 16 shows the M_g versus $u - g$ color-magnitude diagram of our

sample. The coolest DQ white dwarfs in Figure 16 appear to have bluer $u - g$ colors compared to other white dwarfs (see also Figure 2 in Caron et al. 2023); all but one of the DQs have $u - g \leq 1.1$. The exception is SDSS J110548.54–161658.8, which has a relatively large uncertainty in its u -band magnitude. Hence, the coolest DQ white dwarfs may be identified through the use of Gaia parallaxes and SDSS + Pan-STARRS photometry. For example, concentrating on the coolest DQ white dwarfs with $M_g \geq 15$, $u - g \leq 1.0$, and $g - z \geq 0.7$, we find 24 candidates: 12 are spectroscopically confirmed to be DQs, 2 are DCs, and 1 is a DX. Table 3 provides a list of the remaining 9 candidates without follow-up spectroscopy. If confirmed, these objects would demon-

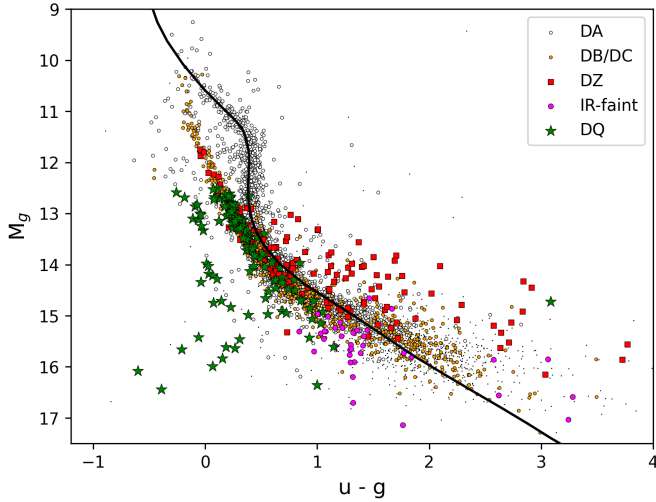


Figure 16. M_g versus $u - g$ color-magnitude diagram of our sample. The symbols are the same as in Figure 14. The dots mark the remaining objects without spectra.

Table 3. Cool DQ white dwarf candidates in the 100 pc SDSS sample that need follow-up spectroscopy to be confirmed.

SDSS name	Gaia SourceID	$u - g$	M_g
J003020.63-180642.5	2364195122092662912	+0.02	15.95
J005155.31-050809.7	2525463206957893248	+0.95	16.07
J011121.89+345940.1	320973385751077376	-0.84	16.68
J013034.00+052656.1	2564860667085575552	+0.49	15.62
J074256.75-124750.3	3030820432081929088	-0.04	15.47
J125047.04+265146.1	3961591831405665280	+0.62	15.78
J125552.90+671244.2	1679189040001914880	-0.31	15.56
J184708.60-021216.0	4259121228365719168	-0.18	15.11
J233118.85+092415.0	2761401084970307712	+0.41	16.18

strate an efficient method for identifying the coolest DQ white dwarfs in the solar neighborhood.

5.2. Global Results

Figure 17 shows the stellar masses as a function of temperature for the spectroscopically confirmed white dwarfs in the 100 pc sample and the SDSS footprint. Our spectroscopic follow-up is 86% complete for white dwarfs hotter than 5000 K. We did not target cooler white dwarfs for spectroscopy, but for completeness we include them in this plot if they have spectra available in the literature. Hence the sudden drop in the number of confirmed white dwarfs below this temperature is due to this observational bias. In addition, we limit this figure to $T_{\text{eff}} < 15,000$ K, since cool white dwarfs dom-

inate our volume-limited sample and this is also where most of the interesting physics happens. We include the theoretical isochrones for C/O-core white dwarfs with thick envelopes, $q(\text{He}) = 10^{-2}$ and $q(\text{H}) = 10^{-4}$. Also shown are the same isochrones where the progenitors lifetimes are taken into account (dotted lines); these are calculated by combining the MESA isochrones (Choi et al. 2016), the initial-final mass relation from Cunningham et al. (2024), and the white dwarf cooling sequences from Bédard et al. (2020). These isochrones match the bottom of the observed sequence well. The solid blue curves mark the onset of crystallization in the core (lower curve) and where 80% of the star has solidified (upper curve), while the dashed curve indicates the onset of convective coupling (Fontaine et al. 2001). The blue dotted curve marks the transition from the classical to the quantum (Debye cooling) regime in the ionic plasma.

Figures similar to this one have been presented in the literature several times before (e.g., Bergeron et al. 2019; Kilic et al. 2020; Caron et al. 2023). What sets this figure apart is that the spectroscopic follow-up here is significantly more complete (down to 5000 K), and also this is a volume-limited sample as opposed to the Caron et al. (2023) sample. The stars enter this diagram on the left, and evolve horizontally to the right as they age. Figure 17 reveals the main peak in the mass distribution at $0.6 M_{\odot}$ and the pile-up of stars on the crystallization sequence. The pile-up is the most significant below 10,000 K, as the more common white dwarfs below $M = 1 M_{\odot}$ start crystallizing.

5.3. DA Mass Distribution

Figure 18 presents the mass distribution of DA white dwarfs with $T_{\text{eff}} \geq 10,000$ K (blue), $T_{\text{eff}} \geq 6000$ K (green), and $T_{\text{eff}} \geq 5000$ K (red histogram) based on 2108 stars best-fit with pure H atmosphere models. The figure also includes the results from fitting two Gaussians to the observed peak and the broad shoulder from massive white dwarfs. For example, for the $T_{\text{eff}} \geq 10,000$ K DA sample, the mass distribution shows a dominant peak at $0.599 M_{\odot}$ with a 1σ spread of only $0.029 M_{\odot}$, whereas the contribution from massive white dwarfs is best-fit with a Gaussian at $0.78 M_{\odot}$. The main peak stays at $0.59 M_{\odot}$ for the entire DA sample, but the broad shoulder from massive DA white dwarfs moves closer to the main peak with decreasing temperature. This is simply a manifestation of the crystallization sequence in the one dimensional mass distribution shown in this figure.

Figure 17 demonstrates that with time, lower mass white dwarfs start crystallizing, and the extra cooling

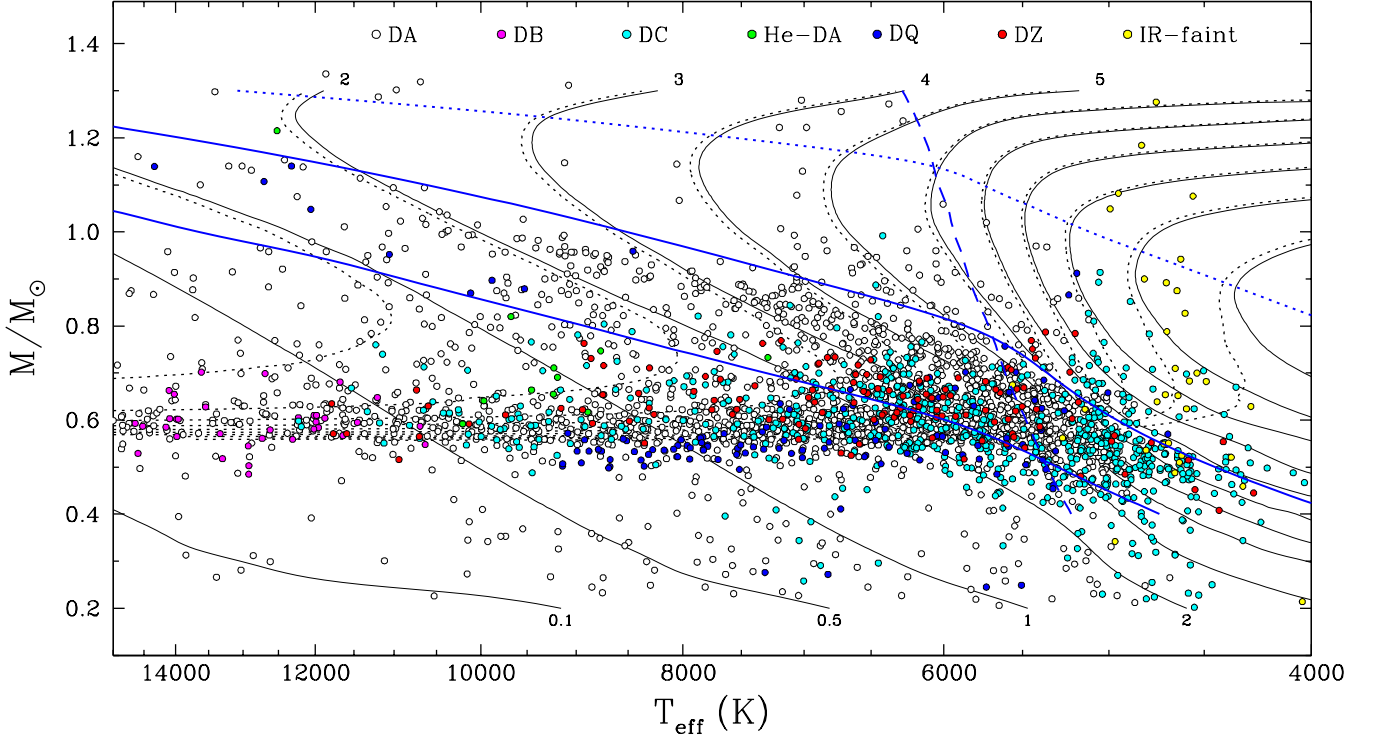


Figure 17. Stellar masses as a function of effective temperature for all spectroscopically confirmed white dwarfs in the 100 pc sample and the SDSS footprint. The solid black curves display theoretical isochrones, labeled in units of Gyr, for C/O-core white dwarfs with $q(\text{He}) = 10^{-2}$ and $q(\text{H}) = 10^{-4}$, and the dotted curves show the same isochrones with the progenitor lifetimes included. The lower blue solid curve marks the onset of crystallization at the center of evolving models, while the upper curve marks the locations where 80% of the total mass has solidified. The dashed curve indicates the onset of convective coupling, while the blue dotted curve corresponds to the transition between the classical to the quantum (Debye cooling) regime in the ionic plasma.

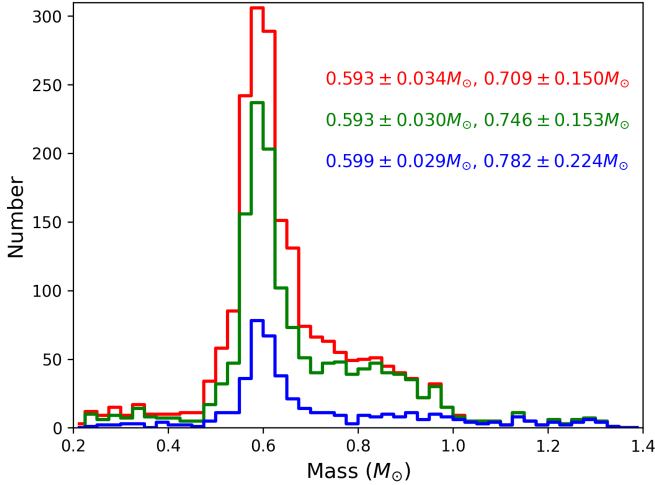


Figure 18. DA white dwarf mass distribution for $T_{\text{eff}} \geq 10,000$ K (blue), $T_{\text{eff}} \geq 6000$ K (green), and $T_{\text{eff}} \geq 5000$ K (red).

delays from crystallization, phase separation, and other associated effects like distillation creates a pile-up. The location of the pile-up moves as a function of temper-

ature. Hence, plotting the DA mass distribution as a one-dimensional histogram (as in Figure 18) leads to a shifting broad shoulder from massive white dwarfs as a function of temperature.

An interesting phenomenon revealed by the DA white dwarf mass distribution is the paucity of ultramassive DA white dwarfs at cooler temperatures. There are 39 DAs (including 1 DAQ) with $M \geq 1.1 M_{\odot}$ and $T_{\text{eff}} \geq 10,000$ K, but only 10 between 6000-10,000 K, and none below 6000 K. It takes 2.2 Gyr for a $1.1 M_{\odot}$ O/Ne-core DA white dwarf to cool down to 10,000 K, but the same star takes 5.0 and 7.0 Gyr to cool down to 6000 and 5000 K, respectively (Camisassa et al. 2019). Hence, based on the standard evolutionary models and assuming a constant star formation rate, we would expect to find nearly a factor of three more ultramassive white dwarfs below 10,000 K. Instead, we see a factor of four less. Hence, ultramassive DA white dwarfs with $M \geq 1.1 M_{\odot}$ are an order of magnitude less common than expected below 10,000 K.

Blouin et al. (2021) showed that ^{22}Ne distillation can lead to ~ 8 Gyr cooling delays in ultramassive white dwarfs, and Bédard et al. (2024) successfully fit the lumi-

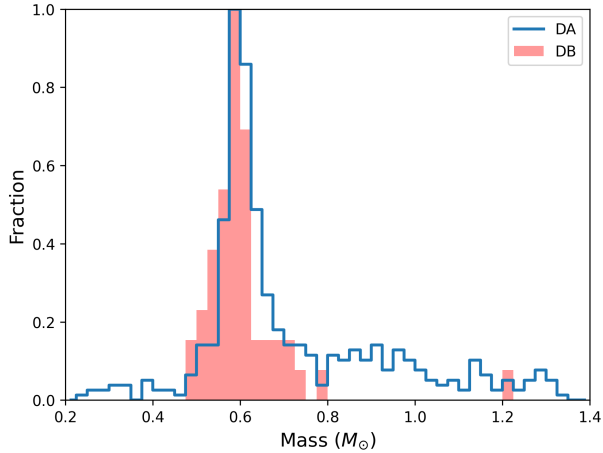


Figure 19. Normalized mass distributions of DAs with $T_{\text{eff}} \geq 10,000$ K and DB white dwarfs in the 100 pc SDSS sample.

osity function of ultramassive white dwarfs assuming a small fraction ($\sim 6\%$) goes through this process. Hence, the paucity of cooler ultramassive white dwarfs in the solar neighborhood can be explained if a fraction of them get stuck on the crystallization sequence due to ^{22}Ne distillation. Because they spend a considerable fraction of the Hubble time on the crystallization sequence, these distilled stars are over-represented on that sequence (see also Cheng et al. 2019; Camisassa et al. 2021).

The lack of ultramassive white dwarfs with $M \geq 1.1 M_{\odot}$ and $T_{\text{eff}} < 6000$ K is also noteworthy because this is where massive white dwarfs enter the Debye cooling regime, visible as nearly horizontal isochrones in the top right portion of Figure 17. In the Debye cooling range, the specific heat decreases with cooling, rapidly depleting the thermal energy reservoir of the star. This is most significant for massive white dwarfs, and the paucity of ultramassive DA white dwarfs below 6000 K is likely due to this process.

5.4. DB Mass Distribution

Figure 19 shows the normalized mass distribution for DB white dwarfs (red histogram). For comparison, we also show the normalized mass distribution for DAs hotter than 10,000 K (blue histogram). Best-fitting Gaussians have $M = 0.586 M_{\odot}$ and $\sigma = 0.036 M_{\odot}$ for DB white dwarfs, compared to $M = 0.599 M_{\odot}$ and $\sigma = 0.029 M_{\odot}$ for DAs. The peaks of the two distributions are remarkably similar (see also Genest-Beaulieu & Bergeron 2019; Tremblay et al. 2019a).

The mass distribution for DB white dwarfs does not have the high mass tail seen for DAs, as there is only a single DB with $M > 0.8 M_{\odot}$ in our sample, GD 229, which is also magnetic (Jordan et al. 1998). Genest-

Beaulieu & Bergeron (2019) identified four massive DBs in the SDSS spectroscopy sample (see their Figure 12). All four stars are beyond 100 pc, and therefore not included in our sample. However, all four objects have $M \sim 0.8 M_{\odot}$. Jewett et al. (2024) found six DBs with $M \geq 0.9 M_{\odot}$ in the 100 pc sample and the Pan-STARRS footprint, but again, none of those ultramassive DBs are normal; they are either strongly magnetic and/or rapidly rotating. Hence, besides the few ultramassive DBs that are likely merger remnants, the ‘normal’ DBs have masses ranging from 0.5 to 0.8 M_{\odot} . The lack of a high mass tail in the DB population favors single star progenitors (Hallakoun et al. 2024).

5.5. DQ and DZ Mass Distributions

Helium lines become invisible below about 11,000 K. Hence, we would expect DB white dwarfs to turn into DCs when they cool below 11,000 K. However, convective dredge up of C can turn them into DQs, if enough C is brought up to the surface to be visible in optical or UV spectra (Pelletier et al. 1986). Alternatively, metal accretion can turn DCs and DQs into DZs (Blouin 2022).

DC white dwarfs make up the majority of the non-DA white dwarfs in our volume-limited sample, and their mass distribution depends on the amount of H in the atmosphere, as shown in Figure 7. In other words, it is adjusted to match the average mass for DA and DB white dwarfs. Based on the prescription used in our analysis, the DC mass distribution peaks at $M = 0.61 M_{\odot}$ with $\sigma = 0.06 M_{\odot}$ in the $T_{\text{eff}} = 6500\text{-}9500$ K range. This temperature range avoids the issues with model fits to cooler DC white dwarfs (Caron et al. 2023; O’Brien et al. 2024).

Figure 20 shows the mass distributions of classical DQs (excluding warm DQs) and DZs (top panel), and those restricted to the effective temperature range of 6500-9500 K (bottom panel). Out of the 276 He-atmosphere white dwarfs with T_{eff} between 6500-9500 K, the fraction of DC, DQ, and DZ white dwarfs are 54%, 25%, and 18%, respectively. He-DAs make up the rest (3%). As discussed in Section 5.1, DZ white dwarfs follow the DC sequence in Pan-STARRS color-magnitude diagrams, and their mass distribution is similar with $M, \sigma = (0.635, 0.062) M_{\odot}$. On the other hand, DQ white dwarfs stand out in their mass distribution with $M, \sigma = (0.538, 0.025) M_{\odot}$. The relatively tight sequence of DQ white dwarfs observed in color-magnitude diagrams manifests itself as a relatively tight sequence in mass in Figures 17 and 20.

The mass distribution for the classical (or cool) DQs in our sample appears to be shifted towards lower masses compared to all other types. This is not a new result.

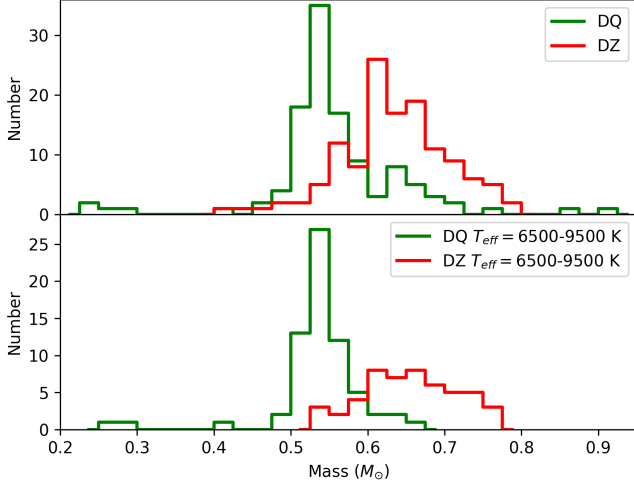


Figure 20. Mass distributions of all classical DQs and DZs (top panel), and those with $T_{\text{eff}} = 6500\text{-}9500$ K (bottom panel).

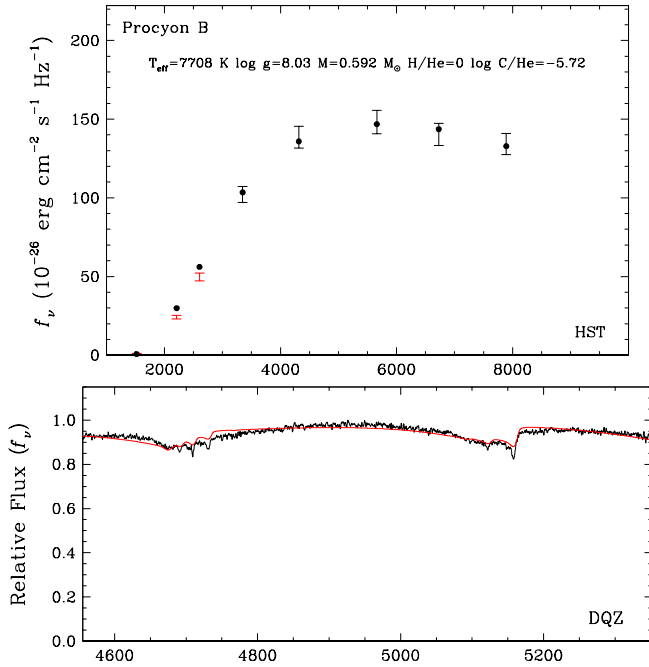


Figure 21. Our model fit to Procyon B. The best-fitting model provides an identical solution to the dynamical mass measurement of $0.592 \pm 0.006 M_{\odot}$ from Bond et al. (2015).

Coutu et al. (2019) found a similar systematic shift in the mass distribution for their larger sample of cool DQ white dwarfs, where they found the peak of the distribution at $0.55 M_{\odot}$. However, they attributed this shift to potential problems with the DQ atmosphere models. They suggested that problems with C opacities in the UV could be one of the possible explanations. They also highlighted the difference between their mass mea-

surement of $M = 0.554 \pm 0.013 M_{\odot}$ for the nearby DQ white dwarf Procyon B and the dynamical mass measurement of $M = 0.592 \pm 0.006 M_{\odot}$ from Bond et al. (2015) as evidence of systematic problems in the atmosphere models.

To investigate this issue further, we have re-analyzed the HST WFPC2 photometry of Procyon B from Provencal et al. (1997), where we used the HST WFPC2 Planetary Camera filter transmission profiles and re-determined the zero points for each filter using the most recent STIS spectrum of Vega. We have calculated the synthetic fluxes using the same filter bandpasses, and used the HST photometry and spectroscopy from Provencal et al. (1997, 2002) to model the spectral energy distribution.

Figure 21 shows the results from this experiment. A model with $T_{\text{eff}} = 7708$ K, $M = 0.592 M_{\odot}$, and $\log C/\text{He} = -5.72$ provides an excellent match to the HST data. Here, we exclude the three UV filters below 3000 \AA (shown in red) to avoid issues with the C and metal opacities in the UV, but the best-fitting model provides a good match to the observed UV photometry as well. Remarkably, our mass measurement based on a self-consistent model atmosphere analysis provides an identical measurement to the dynamical mass from Bond et al. (2015), and provides further support to the idea that the observed low masses for the classical DQs could be real.

Assuming that DQ mass estimates from the current models are accurate, a K-S test comparing the mass distributions for DQ-DC and DQ-DZ white dwarfs rejects the null hypothesis at high significance. Hence, the mass distribution of DQs is significantly different than those of DC and DZ white dwarfs. Bédard et al. (2022) provides a natural explanation for the lower than average masses of DQ white dwarfs. The convective dredge-up process is mass-dependent; carbon contamination is predicted to be more significant for lower mass white dwarfs (Pelletier et al. 1986; Bédard et al. 2022; Blouin et al. 2023a). Carbon dredge-up likely occurs in most cool helium-dominated atmosphere white dwarfs, but only lower mass white dwarfs are polluted enough to show optical C features leading to the DQ classification.

Figure 22 shows the C abundances for our DQ sample along with the theoretical predictions for convective dredge up of carbon for three different masses (0.55 , 0.60 , and $0.65 M_{\odot}$). For each mass, we show three different predictions for a standard envelope mass of $M_{\text{env}} = 10^{-2} M_{\star}$ and initial carbon mass fractions of $X_{\text{C}} = 0.2, 0.4$, and 0.6 (from bottom to top, note that the sequences include a simple linear extrapolation below $T_{\text{eff}} = 8000$ K). The latter represent the range of

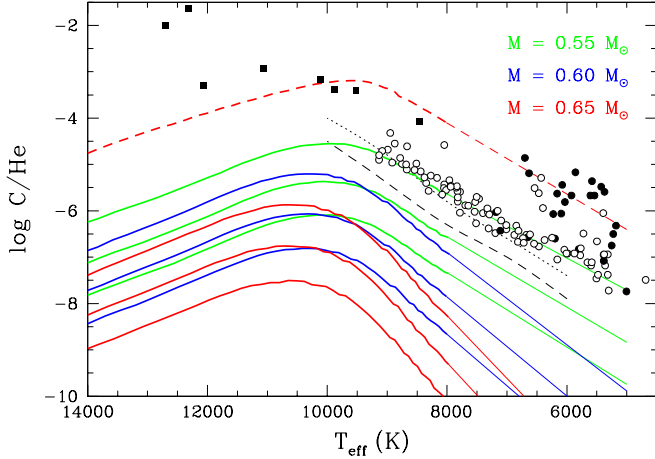


Figure 22. Atmospheric C abundance as a function of temperature for the DQ white dwarfs in our sample. Open and filled circles represent objects with $M < 0.6$ and $\geq 0.6 M_{\odot}$, respectively. The filled squares mark warm DQs that are significantly more massive. Black dotted and dashed lines show the optical spectroscopic detection limits for signal-to-noise ratios of 20 and 50, respectively. The solid lines show the theoretical predictions for the convective dredge-up of carbon for three different masses, initial carbon mass fractions of $X_C = 0.2, 0.4,$ and 0.6 (from bottom to top), and a standard envelope with $M_{\text{env}} = 10^{-2} M_{\star}$. The red dashed line shows the predictions for a $0.65 M_{\odot}$ white dwarf with a thin envelope, $M_{\text{env}} = 10^{-3.5} M_{\star}$. The theoretical predictions stop at $T_{\text{eff}} = 8000$ K and are linearly extrapolated at lower temperatures.

empirically measured carbon mass fractions in PG 1159 stars (Werner & Herwig 2006; Werner & Rauch 2014). The filled circles represent objects with $M \geq 0.6 M_{\odot}$, and the dotted and dashed lines represent the optical spectroscopic detection limit of carbon for typical spectra with signal-to-noise ratios of 20 and 50, respectively.

This figure along with the DQ mass distribution shown in Figure 17 reveal several clues to the origin of DQ white dwarfs, but also raise several questions. The low-mass DQ population (open circles) shows a relatively tight sequence in C/He versus temperature, but there is a larger spread in C abundances for the cooler DQs below 7000 K. The red dashed line shows an evolutionary sequence for a $0.65 M_{\odot}$ white dwarf with a thin envelope, $M_{\text{env}} = 10^{-3.5} M_{\star}$, and an initial carbon mass fraction of $X_C = 0.6$ for its PG 1159 progenitor. There may be two different populations of classical DQ white dwarfs below 7000 K; a low-mass DQ sequence that extends from 9500 K down to 5000 K, and a secondary sequence of $M > 0.6 M_{\odot}$ DQs with a larger spread in mass and C abundance.

The tight sequence of low-mass DQs is presumed to be due to an observational bias, as the bottom of the

sequence coincides with the optical detection limits for carbon in typical spectra with a signal-to-noise ratio of 20. In addition, the trend in the C/He ratio is well matched by the theoretical predictions of element transport in white dwarfs (solid lines in Figure 22, see also Bédard 2024). The composition of the progenitor PG 1159 stars has a significant impact on the predicted C/He ratio; the difference between the PG 1159 carbon mass fractions of 0.2 and 0.6 corresponds to a difference of 2 dex in the final C/He ratio in DQ white dwarfs. The evolutionary sequences shown in Figure 22 demonstrate that the progenitors of DQ white dwarfs are likely at the upper end of this range. This implies that the observed DQ population is only the tip of the expected distribution at a given temperature, and the majority of He-atmosphere white dwarfs have lower C abundances that cannot be detected in the optical, and therefore they appear as DC white dwarfs.

A puzzling feature is the relative lack of an overlap between the DQ and the DZ mass distributions. About 18% of the He-atmosphere white dwarfs with $T_{\text{eff}} = 6500 - 9500$ K are DZ white dwarfs. Blouin (2022) demonstrated that metal accretion onto a DQ white dwarf lowers the atmospheric density, which leads to a significant drop in the C_2 abundance and suppresses the Swan bands so that the star turns into a DZ white dwarf. Given the number of DQ and DC white dwarfs with $M = 0.50 - 0.55$ and $0.5 - 0.6 M_{\odot}$, and if metal accretion occurs in 18%, then we would expect to find 9 and 21 transitioned DZs in the same mass ranges, whereas the observational sample has 3 and 9 DZs, respectively.

The secondary sequence of cool DQs with a larger spread in mass and C abundance can be modeled as $M \sim 0.6 M_{\odot}$ stars, but with a much thinner He-envelope. One of the issues with this interpretation is that we lack progenitors of such stars in our sample at higher effective temperatures. However, there are several potential DQ progenitors in the 7000 – 11,000 K range in Coutu et al. (2019, see their Figure 12), and then there are the DB white dwarfs with similar masses above $T_{\text{eff}} = 11,000$ K. Because our sample is volume-limited, intrinsically rare objects are only seen at cooler temperatures (where there are more stars due to the luminosity function) or on the crystallization branch (where there are more stars due to ^{22}Ne distillation). For example, if these more massive DQs experience a modest cooling delay of a few Gyr (Blouin et al. 2021) on the crystallization sequence, they would be over-represented in this part of the mass-temperature diagram. Of course the discrepancies between the number of low-mass DQ, DC, and DZ white dwarfs could be resolved if the DQ

mass estimates are systematically low, even though the results shown for Procyon B suggest otherwise. Further work on understanding the carbon opacities in the UV and their impact on temperature measurements for DQ white dwarfs would be needed to confirm these results.

Based on these conclusions on the DQ stars, we can now discuss the experiments displayed at the bottom of Figure 7. As mentioned previously in Section 4.4, the location of the B-branch in the Gaia color-magnitude diagram requires DC white dwarfs to have trace amounts of H, C, or other electron donors in their atmospheres, but with C being the most likely culprit. Here we investigate for the very first time whether C and H have the same effect on the analysis of DC stars. The third panel of Figure 7 shows the results (red circles) where all the DC stars in our sample above $T_{\text{eff}} = 6000$ K are analysed with traces of carbon set at the limit of visibility for a signal-to-noise ratio above $S/N = 20$, a value representative of the DQ sample of [Coutu et al. \(2019\)](#), indicated by the dotted line in Figure 22. The results reveal that above ~ 8000 K, the inferred masses are predicted too low, because such large C abundances provide too many free electrons. In contrast, at lower temperatures, the masses are predicted too high, in particular when compared to the predictions from models with traces of hydrogen (two upper panels). Results obtained with a visibility limit of $S/N = 50$, more representative of our 100 pc sample and indicated by the dashed line in Figure 22, are qualitatively similar to those discussed above. Hence, the predictions obtained with an amount of carbon set by the visibility limit and those obtained with a constant trace of hydrogen of $H/He \sim 10^{-5}$ are significantly different.

A possible solution to this problem at high temperatures is to use carbon abundances that are more representative of the He-rich population as a whole, whether C is visible or not. For instance, by using carbon abundances from an average sequence of $0.60 M_{\odot}$ and an initial carbon mass fraction of 0.4 (middle blue sequence in Figure 22), we obtain the results shown in the bottom panel of Figure 7 (note that these are shown only above 8000 K because of the linear extrapolation of the evolutionary sequences in Figure 22 below this temperature). Even though the inferred masses in the 9000–10,000 K temperature range are now closer to the canonical $0.6 M_{\odot}$ value, they increase significantly below 9000 K and merge rapidly with the pure He solutions. We are thus forced to conclude that below $T_{\text{eff}} \sim 9000$ K, electron donors from hydrogen are required to bring the DC masses down, most likely as a result of convective mixing.

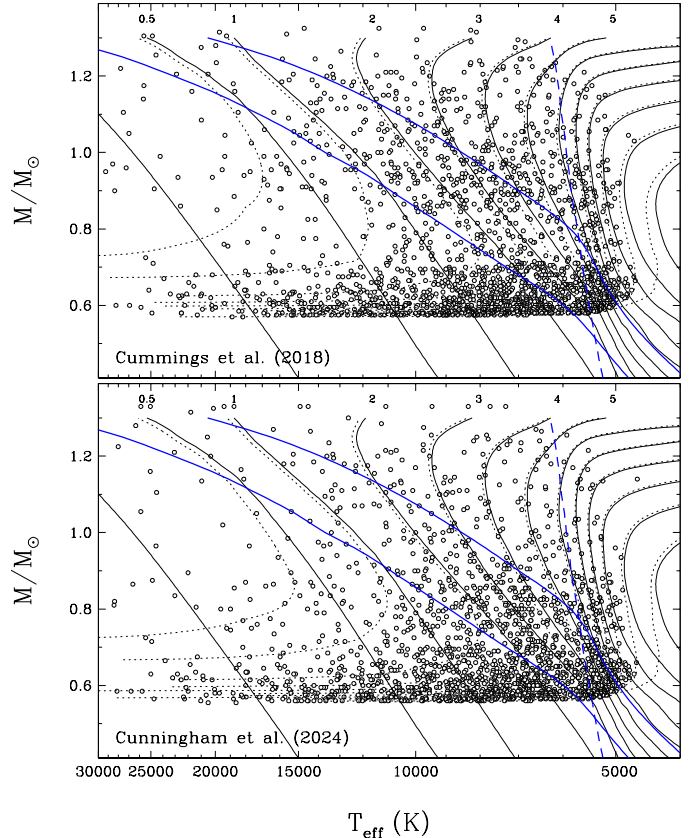


Figure 23. Simulated white dwarf mass and temperature distributions for a 10 Gyr old disk population with a constant star formation rate and the [Cummings et al. \(2018, top panel\)](#) and [Cunningham et al. \(2024, bottom panel\)](#) IFMR. Also shown are the isochrones, crystallization, and convective coupling curves as in Figure 17. We limit this figure to stars hotter than 5000 K, since our follow-up spectroscopy is severely incomplete below that temperature.

5.6. Evolutionary Model Predictions

The mass versus temperature distribution of the 100 pc sample provides important insights into the white dwarf cooling physics. In this section, we provide a comparison between a simulated sample based on the current evolutionary models ([Bédard et al. 2020](#)) and the observed distribution.

Figure 23 shows the mass versus temperature distribution of a simulated DA white dwarf sample for a 10 Gyr old disk population with a constant star formation rate ([Cukanovaite et al. 2023](#)). We limit the simulated sample to objects with $G < 20$ to match Gaia’s limiting magnitude. We also account for spectral evolution by assuming one-third of all DAs below 10,000 K turn into non-DAs, essentially removing them from our simulated sample. The top panel shows the simulation results using the [Cummings et al. \(2018\)](#) initial final mass relation (IFMR) derived from open cluster white dwarfs and the

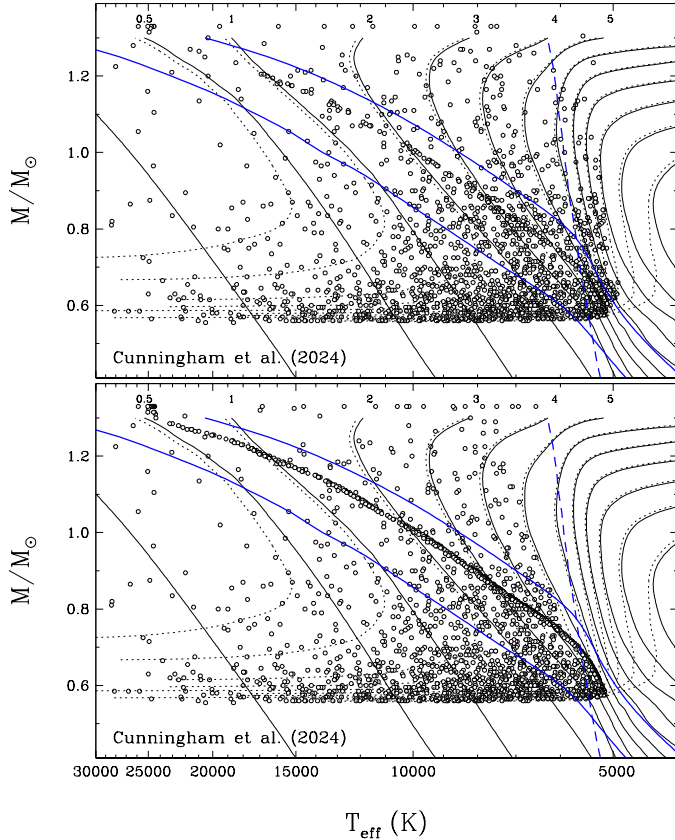


Figure 24. Simulated white dwarf mass and temperature distributions for a 10 Gyr old disk population with a constant star formation rate and the Cunningham et al. (2024) IFMR, where we introduced an extra cooling delay of 1 Gyr (top) and 5 Gyr (bottom panel) at 60% core crystallization.

MIST isochrones (Choi et al. 2016), whereas the bottom panel shows the simulations using the Cunningham et al. (2024) IFMR derived from the volume-complete 40 pc white dwarf sample (O’Brien et al. 2024). The latter closely follows the Cummings et al. (2018) IFMR for initial masses below $3 M_{\odot}$, however there are significant differences between the 3.5 - $5.5 M_{\odot}$ range. For example, Cunningham et al. (2024) predict that a $5.06 M_{\odot}$ star evolves into a $0.91 M_{\odot}$ white dwarf, whereas the Cummings et al. (2018) IFMR gives $1.01 M_{\odot}$ for the same star. These differences manifest themselves in the massive white dwarf population. The Cunningham et al. (2024) IFMR lowers the number of ultramassive white dwarfs with $M \geq 1 M_{\odot}$ and shifts the massive white dwarf population to lower masses due to its shallower slope in the 3.5 - $5.5 M_{\odot}$ range.

Regardless of the IFMR used in these simulations, what is striking is that none of the simulations match the very cool end of the observed sequence (below 5000 K) or the pile-up in the crystallization sequence. The former demonstrates that the coolest white dwarfs are

not modeled properly, even assuming these have H atmospheres (Caron et al. 2023; O’Brien et al. 2024), whereas the latter shows that the evolutionary models are missing important physics. The observed DA sample shows a clear over-density in the crystallization sequence, but the current evolutionary models do not. In addition, the simulated populations still predict relatively large numbers of ultramassive white dwarfs down to 5000 K, yet the 100 pc SDSS sample shows an order of magnitude deficit in the number of ultramassive white dwarfs below 10,000 K.

Bédard et al. (2024) provided a solution to the over-density of the ultramassive Q-branch white dwarfs by including the extra cooling delays from ^{22}Ne distillation only in a small fraction of the white dwarf population (as required by the kinematics). The simulations presented here do not include those cooling delays, but clearly demonstrate that ^{22}Ne distillation is the most likely culprit to explain the observed mass distribution of the DA white dwarfs in the solar neighborhood. Blouin et al. (2021) predict that under the assumption of a more normal ^{22}Ne mass fraction of 0.014, the extra cooling delays from ^{22}Ne distillation occur when $\sim 60\%$ of the interior is crystallized. They predict cooling delays of order 1.8-2 Gyr for 0.6 - $0.8 M_{\odot}$ white dwarfs.

Figure 24 shows the results from a toy model where we introduced extra 1 Gyr (top panel) and 5 Gyr (bottom panel) cooling delays to the stars when their interiors are 60% crystallized. For this toy model, we assume that all white dwarfs experience the same delay. A 1 Gyr extra cooling delay leads to a visible pile-up in the mass versus temperature distribution, and slightly lowers the number of cool and massive white dwarfs, but it is not sufficient to explain the pile-up in the observed population. On the other hand, the 5 Gyr cooling delay leads to a visible pile-up up to 20,000 K, which is much stronger than observed. Such a cooling delay also significantly lowers the number of cool, massive white dwarfs with $M \geq 0.8 M_{\odot}$ as they are stuck on the crystallization sequence. Hence, the answer to explaining the observed pile-up in the white dwarf sequence likely lies in a cooling delay between 1-5 Gyr. This is consistent with the results from Barrientos et al. (2024), who ruled out cooling delays longer than 3.6 Gyr for 0.6 - $0.9 M_{\odot}$ white dwarfs. Even though Barrientos et al. (2024) ruled out the scenario where all white dwarfs experience such a delay; it is still possible that a small fraction of white dwarfs experience a long delay, as in the case of ultramassive white dwarfs.

Our toy model is not physical, in the sense that we arbitrarily added 1 and 5 Gyr cooling delays once the interior reaches the 60% crystallization boundary. A

population synthesis study that uses proper treatment of the cooling delays from ^{22}Ne distillation is required to solve the current discrepancies between the observed and predicted mass and temperature distributions.

5.7. Spectral Evolution: Evidence for Convective Mixing

The surface composition of a non-negligible fraction of white dwarfs changes as they cool, due to various element transport mechanisms, including gravitational settling, radiative levitation, winds, convection, and external accretion. The review article on the spectral evolution of white dwarfs by Bédard (2024) notes that 20-30% of hot white dwarfs have He-rich atmospheres, but this fraction gradually decreases to 5-15% and remains roughly constant between 40,000 and 20,000 K. The He-rich fraction gradually increases back to 20-35% at 10,000 K (see their Figure 2, and Genest-Beaulieu & Bergeron 2019; Ourique et al. 2019; Bédard et al. 2020; Cunningham et al. 2020; López-Sanjuan et al. 2022; Torres et al. 2023; Jiménez-Esteban et al. 2023; Vincent et al. 2024). Based on these fractions, Bédard (2024) estimates that 75% of white dwarfs always retain H atmospheres (though see below), 10% always retain He atmospheres, and the remaining 15% consists of stars that transition from He atmospheres to H atmospheres at high temperatures and then back to He atmospheres at lower temperatures.

The spectral evolution of white dwarfs below $T_{\text{eff}} = 10,000$ K is observationally not well constrained as some studies reported significant increases in the fraction of He-atmosphere white dwarfs below this temperature (e.g. Ourique et al. 2019; Blouin et al. 2019; Torres et al. 2023), while others noted no significant trend. For example, based on a detailed analysis of the volume-complete 40 pc white dwarf sample, O’Brien et al. (2024) found no clear evidence of spectral evolution at the 2σ level between 15,000 and 5000 K. Similarly, studying the $T_{\text{eff}} \leq 10,000$ K white dwarfs in the 100 pc sample, Caron et al. (2023) found no significant evidence of spectral evolution between 10,000 and 6500 K, but noted a drastic increase in the number of He-atmosphere white dwarfs between 6500 and 5500 K. Bédard (2024) stressed that better constraints on the incidence of this spectral transformation are highly desirable.

From a theoretical perspective, we do expect an increase in the number of He-atmosphere white dwarfs below 10,000 K due to convective mixing. In a H-rich white dwarf, the convection zone appears at about an effective temperature of 18,000 K (Cunningham et al. 2019), but it is initially limited to the atmospheric layers. With decreasing temperature, the convection zone deepens, and

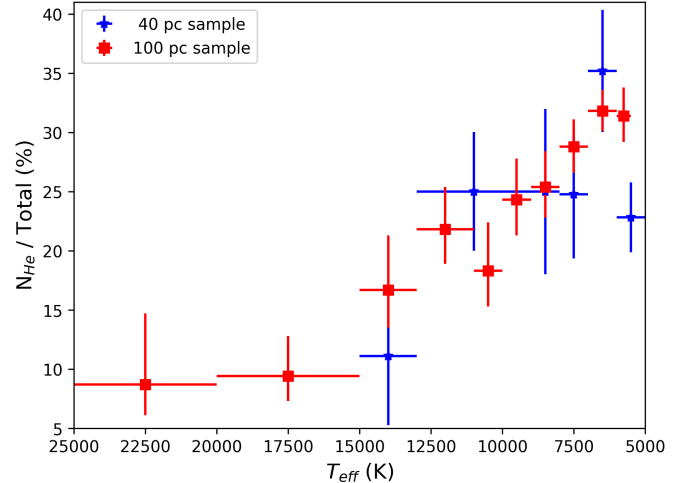


Figure 25. Fraction of He-atmosphere white dwarfs as a function of effective temperature from this work (red points) and the 40 pc sample of O’Brien et al. (2024, blue points).

expands significantly below 12,000 K to include a large portion of the envelope. This process can mix DA white dwarfs with thin surface H layers into He-rich atmosphere white dwarfs. For example, Rolland et al. (2018) estimate that a DA white dwarf with $\log M_H/M_\odot = -13$ would transition to a He-rich atmosphere white dwarf near 12,000 K (see their Table 3), whereas a DA with a thicker H envelope of $\log M_H/M_\odot = -8$ would need to cool down to 7000 K to transition. Hence, depending on the distribution of the H envelope thicknesses in DA white dwarfs, we would expect to see a gradual increase in the He-atmosphere fraction with decreasing temperature.

Figure 25 displays the fraction of He-atmosphere white dwarfs as a function of effective temperature from this work (red points), along with the fractions from the 40 pc sample (O’Brien et al. 2024). We also list the fraction of He-atmosphere white dwarfs in our sample in Table 4. The He-atmosphere fraction in the 40 pc sample was limited to $T_{\text{eff}} \leq 15,000$ K, whereas our sample is big enough to include a large number of stars up to 25,000 K. Given the problems with fitting the spectral energy distributions of cool white dwarfs (see the discussion in O’Brien et al. 2024), we limit this figure to objects with $T_{\text{eff}} \geq 5500$ K, where the atmospheric composition and the physical parameters can be reliably constrained. Here the horizontal error bars represent the width of the temperature bin, and the vertical error bars are calculated based on the Binomial probability distribution.

Figure 25 shows a clear and significant trend in the fraction of He-atmosphere white dwarfs. This fraction

Table 4. Fraction of He-atmosphere white dwarfs as a function of effective temperature.

Temperature Range (10^3 K)	He-fraction (%)
20-25	$8.7^{+6.0}_{-2.6}$
15-20	$9.4^{+3.4}_{-2.1}$
13-15	$16.7^{+4.6}_{-3.2}$
11-13	$21.8^{+3.6}_{-2.9}$
10-11	$18.3^{+4.1}_{-3.0}$
9-10	$24.3^{+3.5}_{-3.0}$
8-9	$25.4^{+3.0}_{-2.6}$
7-8	$28.8^{+2.3}_{-2.2}$
6-7	$31.8^{+1.8}_{-1.7}$
5.5-6	$31.4^{+2.4}_{-2.2}$

goes from 9% between 25,000 and 15,000 K to $24.3^{+3.5}_{-3.0}\%$ at 9500 K, and to $31.8^{+1.8}_{-1.7}\%$ at 6500 K. Note that the increase in the He-fraction is gradual, and it only changes by 7.5 percentage points below 10,000 K. Such a small change can only be reliably measured based on a large sample of white dwarfs. Note that our measurements (red points) are consistent with the constraints from the 40 pc sample (blue points) within the errors. Given the relatively large errors in the He-fraction from the 40 pc sample, it is not surprising that O’Brien et al. (2024) did not find evidence of spectral evolution in their sample.

The observed gradual increase in the He-atmosphere fraction from 10% to about 30% between 20,000 and 6000 K indicate that the underlying DA white dwarf population that transitioned into non-DA white dwarfs had a range of surface H envelope thicknesses; the thicker the H layer, the cooler the mixing temperature. This fraction seems to level out below 6000 K, since the bottom of the convection zone cannot go deeper (see Figure 19 of Bergeron et al. 2022). There is growing evidence that most cool white dwarfs have H dominated atmospheres (Kowalski & Saumon 2006; Bergeron et al. 2019; Kilic et al. 2020; Caron et al. 2023; O’Brien et al. 2024), though given the issues with our understanding of cool white dwarf atmospheres, we refrain from further discussion of spectral evolution beyond $T_{\text{eff}} = 5500$ K.

Given the superior constraints on the fraction of He-atmosphere white dwarfs at cooler temperatures, we can now revise the estimates on the fraction of white dwarfs that transition. We find a minimum He-atmosphere ratio of $\sim 10\%$ and a maximum ratio of $\sim 30\%$, which is also consistent with the fraction of hot white dwarfs

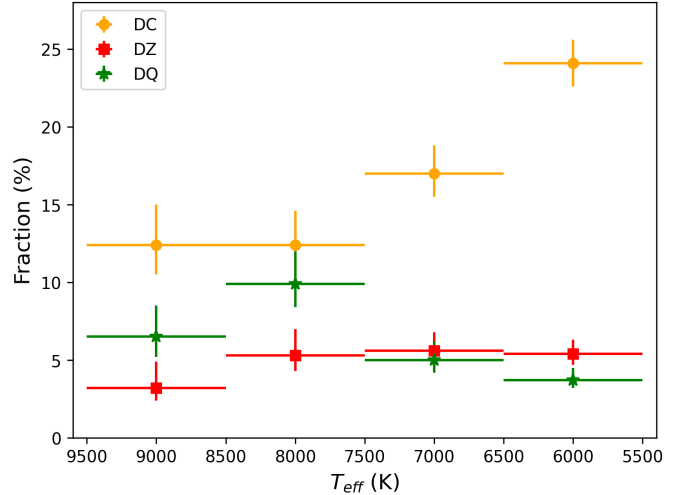


Figure 26. The fraction of DC, DQ, and DZ white dwarfs as a function of effective temperature.

with He-rich atmospheres (20-30%). Hence, we estimate that $\approx 70\%$ of white dwarfs always retain H atmospheres, 10% always retain He atmospheres, and the remaining 20% consists of stars that transition from DO white dwarfs to DAs with thin H layers, which are then convectively mixed at cooler temperatures.

Figure 26 presents the fraction of DC, DQ, and DZ white dwarfs as a function of effective temperature. The number of DC white dwarfs increases significantly below 10,000 K with decreasing temperature, providing direct evidence that DA white dwarfs are transformed into DC white dwarfs through convective mixing. In addition, if the metal accretion rates stay the same with cooling age, we would also expect to see an increase in the number of DZ white dwarfs, as metal accretion onto the increasingly larger population of DC white dwarfs would turn them into DZs. Yet, we see a relatively constant fraction of DZs, meaning that the metal accretion rates onto cool white dwarfs likely decrease with age (but also see Hollands et al. 2018; Blouin & Xu 2022).

5.8. The End of the DQ Sequence

A striking revelation in Figure 26 is that DQ white dwarfs slowly disappear with decreasing temperature. Extending this figure to even cooler temperatures confirms this trend. Our sample has 23, 29, 28, and 31 DQ white dwarfs in the T_{eff} ranges of 9000-8000, 8000-7000, 7000-6000, and 6000-5000 K, respectively. However, there is only 1 DQ white dwarf in our sample below 5000 K; SDSS J124739.05+064604.6 with $T_{\text{eff}} = 4685$ K and $\log C/\text{He} = -7.49$. Admittedly, our spectroscopic survey is biased towards hotter white dwarfs. Nevertheless, we find 163 DC white dwarfs below 5000 K based mostly on the literature spectra, but only 1 DQ. The coolest

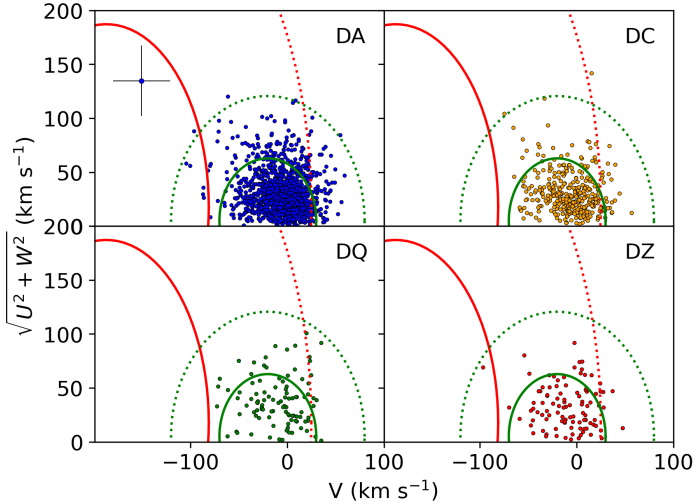


Figure 27. Toomre diagram for DA, DC, DQ, and DZ white dwarfs with $T_{\text{eff}} = 5500\text{--}10,000$ K. Representative error bars are shown for one of the halo white dwarfs, J1240–2317, in the top left panel.

DQ white dwarfs have among the strongest molecular bands. Hence, objects like SDSS J124739.05+064604.6 would certainly be detectable at much lower temperatures. Yet there seems to be this abrupt cut off in the number of DQ white dwarfs below 5000 K. This discrepancy is not unique to our sample (Coutu et al. 2019; Blouin et al. 2019; Bédard 2024).

A search on the MWDD (Dufour et al. 2017) finds 406 DC white dwarfs with $T_{\text{eff}} \leq 5000$ K, but only 6 DQs in the same temperature range. Hence, we are forced to conclude that either they transform into some other spectral type or that because of their lower-than-average masses, their progenitor main-sequence lifetimes are so long that they do not have time to evolve to very low temperatures (see the isochrones that include the progenitor lifetimes in Figure 17). A non-DA star of $0.55 M_{\odot}$ has a total age of 11.9 ± 2.0 Gyr (where the uncertainty is dominated by the IFMR) at $T_{\text{eff}} = 5000$ K. Hence, such stars do not have time to cool down to cooler temperatures. If this scenario is correct, then cool DQs may also display unusual kinematics compared to other white dwarfs with similar temperatures.

Figure 27 shows the Toomre diagram for DA, DC, DQ, and DZ white dwarfs with $T_{\text{eff}} = 5500 - 10,000$ K, along with the 1σ (solid) and 2σ (dotted) velocity ellipsoid values for the thick-disk and halo (Chiba & Beers 2000). We compute Galactic UVW velocities using Gaia parallax and proper motion. Since we do not have radial velocity constraints (DC white dwarfs have no detectable features, for example), we assume zero radial velocity. The tangential velocities clearly center on the

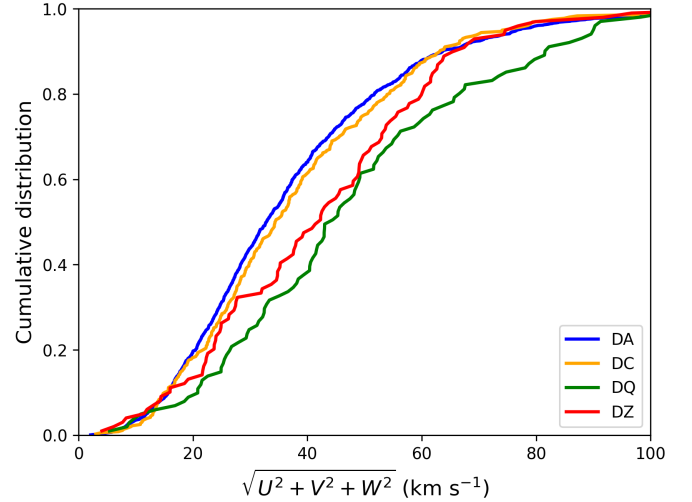


Figure 28. Cumulative distribution of space velocities for DA, DC, DQ, and DZ white dwarfs with $T_{\text{eff}} = 5500\text{--}10,000$ K.

disk, except for three objects that are clearly members of the halo; J0148–1712, J1240–2317, and J1045+5904 (which is a DQ). This motivated us to draw hypothetical radial velocities from the radial component of the thick-disk velocity ellipsoid, 10,000 times for each star. The mean radial velocity of each star remains zero, but the dispersion provides a quantitative measure of how plausible radial velocities may impact the kinematics. Radial velocities project into different UVW velocity components depending on a star’s location on the sky. For completeness, we also redraw the measured proper motions and parallaxes using the full Gaia covariance matrix.

DA and DC white dwarfs have similar velocity distributions in Figure 27; the majority of DAs and DCs are concentrated within the 1σ ellipsoid for thick disk. Comparing the mean UVW dispersions where a set of objects with UVW dispersion identical to Chiba & Beers (2000) thick disk ellipsoid would have a value of 1, DA and DC white dwarfs both have mean values of 1.30, whereas DQs have 1.45. DQs display the broadest velocity distribution among all white dwarfs, and DZs are in between DA/DC and DQs.

Figure 28 shows the cumulative distributions of space velocities of the same stars (see also Farihi et al. 2024). DQs show a distinctive lack of lower ($< 20 \text{ km s}^{-1}$) velocity objects and a greater proportion of higher ($> 50 \text{ km s}^{-1}$) velocity objects. For example, 39% of DQs have total velocities above 50 km s^{-1} , compared to 24% for DAs and 25% for DCs. A K-S test shows that DQ velocity distribution is significantly different than DAs and DCs. Hence, the kinematics of the classical DQs

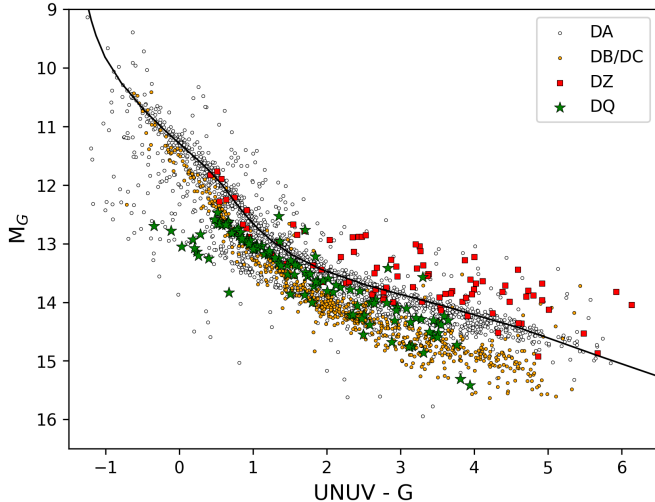


Figure 29. Simulated ULTRASAT-Gaia color-magnitude diagram for the spectroscopically confirmed white dwarfs in the 100 pc sample and the SDSS footprint. The solid line shows the evolutionary sequence for a $0.6 M_{\odot}$ pure H atmosphere white dwarf.

are consistent with a larger contribution of lower-mass and hence older thick disk objects. Larger and more spectroscopically complete surveys of white dwarfs with $T_{\text{eff}} < 5000$ K would be useful for understanding the spectral evolution of DQ white dwarfs at cooler temperatures.

5.9. Looking to the Future: ULTRASAT

We conclude this section by taking advantage of our well defined sample of spectroscopically confirmed white dwarfs in the 100 pc and the SDSS footprint to make predictions for the upcoming ULTRASAT mission. The Ultraviolet Transient Astronomy Satellite (ULTRASAT) will be launched in late 2027 to carry out a wide-field survey of transient and variable sources in an NUV band covering 230-290 nm (Shvartzvald et al. 2024). In addition to high-cadence observations, ULTRASAT will provide an all-sky NUV catalog down to 23.5 ABmag, over 10 times deeper than GALEX. Given its depth, the all sky survey will detect the majority of white dwarfs with $T_{\text{eff}} \geq 5000$ K in the Gaia white dwarf catalog of Gentile Fusillo et al. (2021).

Figure 29 shows a simulated ULTRASAT - Gaia color-magnitude diagram of the spectroscopically confirmed white dwarfs in our sample down to a limiting magnitude of $\text{NUV} = 23.5$. We use the observed Gaia photometry and astrometry along with the simulated ULTRASAT magnitudes. We ignore extinction since our sample is located within 100 pc. GALEX provided NUV photometry for 48% of these white dwarfs, whereas ULTRASAT will detect 89% of this sample, including 87% of the DA

white dwarfs. A combination of Gaia photometry with ULTRASAT’s NUV filter will provide a color-spread of 7 mag for the white dwarf population. The addition of UV photometry will significantly improve the statistical errors in the model fits, especially for hot white dwarfs (Wall et al. 2023).

NUV observations of DZ white dwarfs are more difficult, since they are significantly fainter in the UV due to various metal lines. Our simulations show that about 1/3 of the 100 pc DZ sample will be too faint for ULTRASAT’s all-sky survey. Nevertheless, we predict a relatively large spread in $\text{NUV} - G$ colors of cool white dwarfs, which can help distinguish DZ white dwarfs based on NUV photometry.

DA white dwarfs with pure H atmospheres can serve as excellent flux standards in the UV given their predictable atmospheres. GALEX observed 18 white dwarfs as standard stars, though its photometric calibration relies primarily on the dimmest star in that sample, LDS 749b, as all of the other standard stars were saturated. Wall et al. (2019) verified the absolute flux calibration and extinction coefficients for GALEX using DA white dwarfs with high signal-to-noise ratio spectra and Gaia parallaxes. We include the predicted ULTRASAT NUV magnitudes for our white dwarf sample in Table 2. The DA white dwarfs in our sample can be used to verify the absolute flux calibration for the ULTRASAT mission.

6. CONCLUSIONS

We present the results from a spectroscopic survey of the 100 pc white dwarf sample in the SDSS footprint. In paper I (Kilic et al. 2020), our follow-up targeted white dwarfs with effective temperatures above 6000 K. Here, we extend this survey to cooler white dwarfs with $T_{\text{eff}} \geq 5000$ K. We obtained follow-up spectroscopy of 840 white dwarfs for this work. Combining our new data with the literature data, we now have spectral classifications for 75% of the 4214 white dwarfs in the 100 pc SDSS sample. More importantly, our spectroscopic follow-up is 91% and 86% complete for $T_{\text{eff}} \geq 6000$ and 5000 K, respectively.

We identify 2108 DA white dwarfs with pure H atmospheres. As found in earlier studies based on Gaia astrometry (Kilic et al. 2020; O’Brien et al. 2024), the mass distribution shows a narrow peak at $\approx 0.6 M_{\odot}$ with a broad shoulder from massive white dwarfs. The mass versus temperature distribution of this sample clearly demonstrates that the broad shoulder is due to the pile-up of massive white dwarfs on the crystallization sequence. In addition, ultramassive DA white dwarfs with $M \geq 1.1 M_{\odot}$ are an order of magnitude less common

than expected below 10,000 K. This is likely a natural outcome of the ^{22}Ne distillation process which causes a fraction of ultramassive white dwarfs to be stuck on the crystallization sequence for ~ 10 Gyr (Bédard et al. 2024).

Even though DA white dwarfs are common in the effective temperature range of 5000-6000 K, we do not find any ultramassive DA white dwarfs with $M \geq 1.1 M_{\odot}$ and $T_{\text{eff}} \leq 6000$ K in our sample. Evolutionary models predict that such stars enter the Debye cooling range, which significantly speeds up their evolution. The paucity of $M \geq 1.1 M_{\odot}$ DAs below 6000 K is consistent with these stars rapidly fading away.

We detect a significant trend in the fraction of He-atmosphere white dwarfs as a function of temperature. The fraction increases from 9% at 20,000 K to $\approx 32\%$ at 6000 K. The number of DC white dwarfs increases significantly below 10,000 K with decreasing temperature, providing direct evidence that DA white dwarfs are transformed into DC white dwarfs through convective mixing.

We also detect a relatively tight sequence of DQ white dwarfs in color-magnitude diagrams for the first time. We discuss the implications of this discovery for the DQ mass distribution, though further work on understanding the carbon opacities in the UV and their impact on temperature (and therefore radius and mass) measurements for DQ white dwarfs is needed to confirm these results.

Further progress requires larger spectroscopically complete and volume-limited surveys that can be performed using multi-fiber spectrographs. There are several current and upcoming spectroscopic surveys that are targeting large numbers of white dwarfs. The Dark Energy Spectroscopic Instrument (DESI) Milky Way Survey (Allende Prieto et al. 2020; Manser et al. 2024), the SDSS-V Milky Way Mapper (Kollmeier et al. 2019), the WHT Enhanced Area Velocity Explorer (WEAVE, Jin et al. 2022), and the 4-metre Multi-Object Spectroscopic Telescope (4MOST, de Jong 2019) will target many of the white dwarfs in the Gentile Fusillo et al. (2021) catalog. These surveys offer an opportunity to establish a homogeneous spectroscopic sample of white dwarfs for the first time. The large sample size will enable the identification of rare white dwarf species (like DAQ white dwarfs for example, Jewett et al. 2024; Kilic

et al. 2024), and likely lead to many unexpected discoveries.

We thank J. Rupert for obtaining the MDM data as part of the OSMOS queue. This work is supported in part by the NSF under grant AST-2205736, the NASA under grants 80NSSC22K0479, 80NSSC24K0380, and 80NSSC24K0436, the NSERC Canada, the Fund FRQ-NT (Québec), the Canadian Institute for Theoretical Astrophysics (CITA) National Fellowship Program, the Smithsonian Institution, and by the European Research Council (ERC) under the European Union’s Horizon 2020 research and innovation programme (grant agreement no. 101002408).

The Apache Point Observatory 3.5-meter telescope is owned and operated by the Astrophysical Research Consortium.

Based on observations obtained at the MMT Observatory, a joint facility of the Smithsonian Institution and the University of Arizona.

This paper includes data gathered with the 6.5 meter Magellan Telescopes located at Las Campanas Observatory, Chile.

This work is based on observations obtained at the MDM Observatory, operated by Dartmouth College, Columbia University, Ohio State University, Ohio University, and the University of Michigan. The authors are honored to be permitted to conduct astronomical research on Iolkam Du’ag (Kitt Peak), a mountain with particular significance to the Tohono O’odham.

Based on observations obtained at the international Gemini Observatory, a program of NSF’s NOIRLab, which is managed by the Association of Universities for Research in Astronomy (AURA) under a cooperative agreement with the National Science Foundation on behalf of the Gemini Observatory partnership: the National Science Foundation (United States), National Research Council (Canada), Agencia Nacional de Investigación y Desarrollo (Chile), Ministerio de Ciencia, Tecnología e Innovación (Argentina), Ministério da Ciência, Tecnologia, Inovações e Comunicações (Brazil), and Korea Astronomy and Space Science Institute (Republic of Korea).

Facilities: ARC 3.5m (KOSMOS spectrograph), FLWO 1.5m (FAST spectrograph), Gemini (GMOS spectrograph), Magellan:Baade (MagE spectrograph), MDM (OSMOS), MMT (Blue Channel spectrograph)

REFERENCES

- Allende Prieto, C., Cooper, A. P., Dey, A., et al. 2020, Research Notes of the American Astronomical Society, 4, 188
- Barrientos, M., Kilic, M., Bergeron, P., et al. 2024, ApJ, 973, 88

- Bédard, A. 2024, *Ap&SS*, 369, 43
- Bédard, A., Bergeron, P., & Brassard, P. 2022, *ApJ*, 930, 8
- Bédard, A., Bergeron, P., Brassard, P., & Fontaine, G. 2020, *ApJ*, 901, 93
- Bédard, A., Bergeron, P., & Fontaine, G. 2017, *ApJ*, 848, 11
- Bédard, A., Blouin, S., & Cheng, S. 2024, *Nature*, 627, 286
- Bergeron, P., Dufour, P., Fontaine, G., et al. 2019, *ApJ*, 876, 67
- Bergeron, P., Kilic, M., Blouin, S., et al. 2022, *ApJ*, 934, 36
- Bergeron, P., Leggett, S. K., & Ruiz, M. T. 2001, *ApJS*, 133, 413
- Bergeron, P., Wesemael, F., Dufour, P., et al. 2011, *ApJ*, 737, 28
- Bianchi, L., Shiao, B., & Thilker, D. 2017, *ApJS*, 230, 24
- Blouin, S. 2020, *MNRAS*, 496, 1881
- . 2022, *A&A*, 666, L7
- Blouin, S., Bédard, A., & Tremblay, P.-E. 2023a, *MNRAS*, 523, 3363
- Blouin, S., Daligault, J., & Saumon, D. 2021, *ApJL*, 911, L5
- Blouin, S., & Dufour, P. 2019, *MNRAS*, 490, 4166
- Blouin, S., Dufour, P., Thibeault, C., & Allard, N. F. 2019, *ApJ*, 878, 63
- Blouin, S., Kilic, M., Bédard, A., & Tremblay, P.-E. 2023b, *arXiv e-prints*, arXiv:2307.14295
- Blouin, S., & Xu, S. 2022, *MNRAS*, 510, 1059
- Bond, H. E., Gilliland, R. L., Schaefer, G. H., et al. 2015, *ApJ*, 813, 106
- Camisassa, M., Torres, S., Hollands, M., et al. 2023, *A&A*, 674, A213
- Camisassa, M. E., Althaus, L. G., Torres, S., et al. 2021, *A&A*, 649, L7
- Camisassa, M. E., Althaus, L. G., Córscico, A. H., et al. 2019, *A&A*, 625, A87
- Caron, A., Bergeron, P., Blouin, S., & Leggett, S. K. 2023, *MNRAS*, 519, 4529
- Cheng, S., Cummings, J. D., & Ménard, B. 2019, *ApJ*, 886, 100
- Chiba, M., & Beers, T. C. 2000, *AJ*, 119, 2843
- Choi, J., Dotter, A., Conroy, C., et al. 2016, *ApJ*, 823, 102
- Coutu, S., Dufour, P., Bergeron, P., et al. 2019, *ApJ*, 885, 74
- Cukanovaite, E., Tremblay, P. E., Toonen, S., et al. 2023, *MNRAS*, 522, 1643
- Cummings, J. D., Kalirai, J. S., Tremblay, P. E., Ramirez-Ruiz, E., & Choi, J. 2018, *ApJ*, 866, 21
- Cunningham, T., Tremblay, P.-E., Freytag, B., Ludwig, H.-G., & Koester, D. 2019, *MNRAS*, 488, 2503
- Cunningham, T., Tremblay, P.-E., Gentile Fusillo, N. P., Hollands, M., & Cukanovaite, E. 2020, *MNRAS*, 492, 3540
- Cunningham, T., Tremblay, P.-E., & W. O'Brien, M. 2024, *MNRAS*, 527, 3602
- de Jong, R. 2019, in *Preparing for 4MOST*, 1
- Dufour, P., Bergeron, P., & Fontaine, G. 2005, *ApJ*, 627, 404
- Dufour, P., Blouin, S., Coutu, S., et al. 2017, in *Astronomical Society of the Pacific Conference Series*, Vol. 509, 20th European White Dwarf Workshop, ed. P. E. Tremblay, B. Gaensicke, & T. Marsh, 3
- Dufour, P., Fontaine, G., Liebert, J., Schmidt, G. D., & Behara, N. 2008, *ApJ*, 683, 978
- Dunlap, B. H., & Clemens, J. C. 2015, in *Astronomical Society of the Pacific Conference Series*, Vol. 493, 19th European Workshop on White Dwarfs, ed. P. Dufour, P. Bergeron, & G. Fontaine, 547
- Farihi, J., Dufour, P., & Wilson, T. G. 2024, *MNRAS*, 530, 4446
- Fontaine, G., Brassard, P., & Bergeron, P. 2001, *PASP*, 113, 409
- Gaia Collaboration, Babusiaux, C., van Leeuwen, F., et al. 2018, *A&A*, 616, A10
- Gänsicke, B. T., Rodríguez-Gil, P., Gentile Fusillo, N. P., et al. 2020, *MNRAS*, 499, 2564
- Genest-Beaulieu, C., & Bergeron, P. 2019, *ApJ*, 882, 106
- Gentile Fusillo, N. P., Tremblay, P. E., Cukanovaite, E., et al. 2021, *MNRAS*, 508, 3877
- Hallakoun, N., Shahaf, S., Mazeh, T., Toonen, S., & Ben-Ami, S. 2024, *ApJL*, 970, L11
- Hansen, B. M. S. 1998, *Nature*, 394, 860
- Holberg, J. B., Oswalt, T. D., Sion, E. M., & McCook, G. P. 2016, *MNRAS*, 462, 2295
- Hollands, M. A., Gänsicke, B. T., & Koester, D. 2018, *MNRAS*, 477, 93
- Jewett, G., Kilic, M., Bergeron, P., et al. 2024, *ApJ*, 974, 12
- Jiménez-Esteban, F. M., Torres, S., Rebassa-Mansergas, A., et al. 2023, *MNRAS*, 518, 5106
- . 2018, *MNRAS*, 480, 4505
- Jin, S., Trager, S. C., Dalton, G. B., et al. 2022, *arXiv e-prints*, arXiv:2212.03981
- Jordan, S., Schmelcher, P., Becken, W., & Schweizer, W. 1998, *A&A*, 336, L33
- Kawka, A., Ferrario, L., & Vennes, S. 2023, *MNRAS*, 520, 6299
- Kepler, S. O., Pelisoli, I., Koester, D., et al. 2019, *MNRAS*, 486, 2169
- Kilic, M., Bergeron, P., Blouin, S., et al. 2024, *ApJ*, 965, 159
- Kilic, M., Bergeron, P., Kosakowski, A., et al. 2020, *ApJ*, 898, 84
- Koester, D., & Kepler, S. O. 2019, *A&A*, 628, A102

- Kollmeier, J., Anderson, S. F., Blanc, G. A., et al. 2019, in *Bulletin of the American Astronomical Society*, Vol. 51, 274
- Kowalski, P. M. 2010, *A&A*, 519, L8
- Kowalski, P. M., & Saumon, D. 2006, *ApJL*, 651, L137
- López-Sanjuan, C., Tremblay, P. E., Ederoclite, A., et al. 2022, *A&A*, 658, A79
- Manser, C. J., Izquierdo, P., Gänsicke, B. T., et al. 2024, *arXiv e-prints*, arXiv:2402.18641
- Marsh, T. R., Dhillon, V. S., & Duck, S. R. 1995, *MNRAS*, 275, 828
- McCleery, J., Tremblay, P.-E., Gentile Fusillo, N. P., et al. 2020, *MNRAS*, 499, 1890
- Munday, J., Pelisoli, I., Tremblay, P. E., et al. 2024, *MNRAS*, 532, 2534
- O'Brien, M. W., Tremblay, P. E., Gentile Fusillo, N. P., et al. 2023, *MNRAS*, 518, 3055
- O'Brien, M. W., Tremblay, P. E., Klein, B. L., et al. 2024, *MNRAS*, 527, 8687
- Ourique, G., Romero, A. D., Kepler, S. O., Koester, D., & Amaral, L. A. 2019, *MNRAS*, 482, 649
- Pelletier, C., Fontaine, G., Wesemael, F., Michaud, G., & Wegner, G. 1986, *ApJ*, 307, 242
- Press, W. H., Flannery, B. P., & Teukolsky, S. A. 1986, *Numerical recipes. The art of scientific computing*
- Provencal, J. L., Shipman, H. L., Koester, D., Wesemael, F., & Bergeron, P. 2002, *ApJ*, 568, 324
- Provencal, J. L., Shipman, H. L., Wesemael, F., et al. 1997, *ApJ*, 480, 777
- Rolland, B., Bergeron, P., & Fontaine, G. 2018, *ApJ*, 857, 56
- Saumon, D., Blouin, S., & Tremblay, P.-E. 2022, *Physics Reports*, 988, 1
- Shvartzvald, Y., Waxman, E., Gal-Yam, A., et al. 2024, *ApJ*, 964, 74
- Sion, E. M., Greenstein, J. L., Landstreet, J. D., et al. 1983, *ApJ*, 269, 253
- Torres, S., Cruz, P., Murillo-Ojeda, R., et al. 2023, *A&A*, 677, A159
- Tremblay, P.-E., Bédard, A., O'Brien, M. W., et al. 2024, *New Astronomy Reviews*, 99, 101705
- Tremblay, P. E., Bergeron, P., & Gianninas, A. 2011, *ApJ*, 730, 128
- Tremblay, P. E., Cukanovaite, E., Gentile Fusillo, N. P., Cunningham, T., & Hollands, M. A. 2019a, *MNRAS*, 482, 5222
- Tremblay, P.-E., Fontaine, G., Fusillo, N. P. G., et al. 2019b, *Nature*, 565, 202
- Tremblay, P. E., Hollands, M. A., Gentile Fusillo, N. P., et al. 2020, *MNRAS*, 497, 130
- Vincent, O., Barstow, M. A., Jordan, S., et al. 2024, *A&A*, 682, A5
- Wall, R. E., Kilic, M., Bergeron, P., & Leiphart, N. D. 2023, *MNRAS*, 523, 4067
- Wall, R. E., Kilic, M., Bergeron, P., et al. 2019, *MNRAS*, 489, 5046
- Werner, K., & Herwig, F. 2006, *PASP*, 118, 183
- Werner, K., & Rauch, T. 2014, *A&A*, 569, A99
- Wesemael, F., Greenstein, J. L., Liebert, J., et al. 1993, *PASP*, 105, 761